AIAA SPACE 2010 Conference & Exposition
30 August - 2 September 2010, Anaheim, California

AIAA 2010-8780

Sun and Earth Access Trades for Lunar South Pole Landing Site Selection

Jarret M. Lafleur*
NASA Johnson Space Center, Houston, Texas 77058

and

Casey Heeg†
NASA Jet Propulsion Laboratory, Pasadena, California 91109

One of the leading candidate sites for future lunar exploration is Shackleton Crater, a 20-km-diameter, 4-km-deep depression offset 10 km from the south pole of the Moon. The perpetual darkness that exists at the floor of the crater, which makes it scientifically interesting and a potential supply of resources, is coupled with near-continuous sunlight atop the rim and some of the surrounding area. In order to leverage favorable Sun and Earth access conditions in the region, engineers designing future missions must be able to quantify these access conditions and effectively use this data to select an ideal landing or outpost site. This paper details work completed to develop this capability within Team X at the NASA Jet Propulsion Laboratory using a Satellite Tool Kit (STK) model coupled with a MATLAB site selection tool employing multi-attribute decision-making (MADM) techniques. Three scenarios are analyzed in terms of the fraction of the year for which Sun and Earth access exists, the maximum durations for which access is nonexistent, and access consistency. These multiple metrics are combined into an aggregate suitability score based on user weights and the Technique for Order Preference by Similarity to Ideal Solution (TOPSIS), and optimal sites are identified. In addition, weighting-independent Pareto-optimal points are identified and are shown to be clustered in four geographic regions. The most promising points have access to the Sun 89-93% of the year and to the Earth about 58% of the year. It is shown that access results are highly sensitive to a spacecraft's effective solar array or antenna altitude above the surface. Recommendations of future sites to consider are provided, and avenues for future expansion of this analysis and its tools are identified.

Nomenclature

AHP	=	Analytic Hierarchy Process	*NAOJ*	=	National Astronomical Observatory of Japan
DEM	=	Digital Elevation Map	*SELENE*	=	Selenological and Engineering Explorer
GUI	=	Graphical User Interface	*STK*	=	Satellite Tool Kit
IAU	=	International Astronomical Union	*UTC*	=	Universal Time Coordinated
MADM	=	Multi-Attribute Decision-Making			

I. Introduction

ONE of the leading candidate sites for future robotic and human exploration of the Moon is Shackleton Crater, a 20-km-diameter, 3.5-billion-year-old[1] depression whose center is offset just 10 km from the lunar south pole. The walls of Shackleton rise 4 km from the bottom of the crater, and the result is a crater floor draped in perpetual darkness. Maximum daytime temperatures of the coldest parts of the crater are estimated to be 70 K,[2] and considerable speculation has been made about the accumulation of volatiles such as water ice in this cold trap.

*Graduate Co-op Student, Flight Mechanics and Trajectory Design Branch/EG5, Student Member AIAA.
†Team X Lead Engineer for Trajectory Visualization, Advanced Design Engineering Group/312I.

The possible presence of perpetually dark crater floors, such as those of Shackleton, has been recognized since at least 1952.[3] While hypotheses on the presence of large quantities of water beneath the lunar surface existed in the late 1800s,[4,5] it was in 1961 that the possible presence of appreciable quantities of water ice on crater floors and in similar "cold traps" was seriously examined.[6,7] Such ice could be a useful resource for future lunar outposts, and it is also of scientific interest since it may provide an indication of the degree of chemical differentiation of the Moon itself.[7] In 1996, the Clementine spacecraft's bistatic radar experiment returned observations from permanently shadowed regions of the lunar south pole consistent with the presence of ice deposits.[8,9] Additionally, neutron flux measurements of these regions from the Lunar Prospector spacecraft in 1998 suggested the presence of significant amounts of hydrogen in the form of water ice.[10,11] Most recently, in October 2009 the Lunar Crater Observation and Sensing Satellite (LCROSS)[12] impacted a permanently shadowed region of the lunar south pole's Cabeus crater and revealed an estimated 24 gallons of water over an impact area 20-30 m in diameter.[13]

In addition to science- and resource-driven interest in the south pole region, operational advantages also exist. Just as some crater floors experience perpetual darkness, some crater rims and mountains in the region experience near-constant sunlight. This contrasts with most other locations on the Moon that have 14-day eclipses (i.e., lunar night), and thus such rims and mountains have clear implications for photovoltaic power production. Additionally, some locations in the region are in line of sight with Earth a large fraction of the time, a quality beneficial for radio communication with operators on the ground.

Because of the low elevation angles of the Earth and Sun over the lunar south pole horizon, critical in any study of Sun or Earth access is accurate terrain elevation data. The question of solar illumination at the south pole has been examined many times over the past two decades, often soon after new terrain data becomes available.[8,14-18] A thorough summary of previous efforts is available in Ref. 19. Earth access has been covered to a much smaller degree in the literature, although a number of studies exist exploring options for lunar communications relay satellites and constellations under the assumption that this capability will be necessary.[20-23]

Provided in this paper is an overview of a capability that now exists within the Team X concurrent engineering and conceptual design group at the NASA Jet Propulsion Laboratory to generate Sun and Earth access statistics for the lunar south pole using Satellite Tool Kit (STK). In addition to allowing for detailed examination of a single landing or outpost site, this capability is used to generate Earth and Sun access statistics at thousands of locations in the region surrounding Shackleton Crater. Multi-attribute decision-making (MADM) techniques, including an interactive graphical user interface (GUI), are used to identify acceptable as well as Pareto-optimal candidate sites. This analysis makes use of, but is not limited to, laser altimeter terrain data from the Kaguya (SELENE) spacecraft,[24] and attributes traded include percent Earth access, percent Sun access, maximum Earth eclipse duration, and maximum Sun eclipse duration. All attributes in this study are properties of the lunar environment and do not assume any particular mission or system configuration. As a result, this analysis can be used in support of virtually any future lunar south pole mission.

II. Access Data Generation and Validation

Although the tools developed here can be applied to any properly-formatted lunar topography data, the analysis presented in this paper makes use of publicly-available topography data from the Japan Aerospace Exploration Agency (JAXA) Kaguya (SELENE) mission.[24] This data choice is convenient because it permits validation against previously published illumination analysis.[18] STK is chosen as the analysis engine because of its relatively wide availability in the industry, its extensibility to other applications (e.g., it allows tracking of Earth, the Sun, and if desired, satellites or other man-made objects), and its visualization capabilities. In order to use the JAXA ASCII-formatted topography data within STK, a series of conversions are required, and these are documented here.

A. Access Data Generation

In order to generate Earth and Sun access data based on the Kaguya (SELENE) topography, an STK model is created through a two-step process. In a third step, MATLAB is used to interface with STK to automate analysis of a swath of latitude/longitude coordinates in order to map access statistics.

1. ASCII-to-DEM Conversion

The original Kaguya (SELENE) south pole topography data extends from 85.0078°S to 89.9921°S at a resolution of 0.0156° (473.8 m) and from 179.9111°W to 179.9111°E at a resolution of 0.177865° (469.3 m at the northern extent of the map; 0.7 m at the southern extent). The data is in a three-column (longitude/latitude/elevation) ASCII format that STK will not recognize. STK will, however, recognize terrain data

in the U.S. Geological Survey (USGS) DEM file format. The commercially-available Global Mapper 10 software package is used to accomplish this conversion. In this conversion process, elevations are rounded to the nearest meter, and the reference for the DEM projection is the WGS84 coordinate system (due to an STK requirement for lunar terrain). In addition, because of an STK terrain modeling limitation, the entire terrain data set is offset in altitude by +10 km to prevent obscuration from a false wall-like feature that would otherwise exist at the 180° anti-meridian. The effect of this 10 km offset on Earth and Sun access results is expected to be negligible given the large distances to the Earth and Sun. Figure 1 shows an adaptation of the terrain elevation map in Global Mapper, and Fig. 2 shows this map overlayed with names of regional features.

2. STK Analysis

Within an STK 8 scenario, the DEM from Step 1 is imported and assigned to the Moon. A facility is placed at a given latitude/longitude coordinate, and elevation is determined from the supplied DEM terrain. An azimuth-elevation mask is created and activated as a constraint to prevent line-of-sight through terrain. Earth and the Sun are created in the scenario, and access is computed between the facility and the centers of the Earth and Sun over a one-year time period using the STK default of DE405 ephemeris and the IAU 2000 lunar orientation and rotational elements. Access periods are computed to a precision within fractions of a second. The access analysis can be exported in a text format or through MATLAB, as is discussed shortly. Although not required in order to produce numerical data, STK also has a visualization capability; in order to use this capability, the DEM file can be converted to PDTT and JP2 files and rendered in a 3-D graphics window. An example 3-D visualization along with a sample access report is shown in Fig. 3.

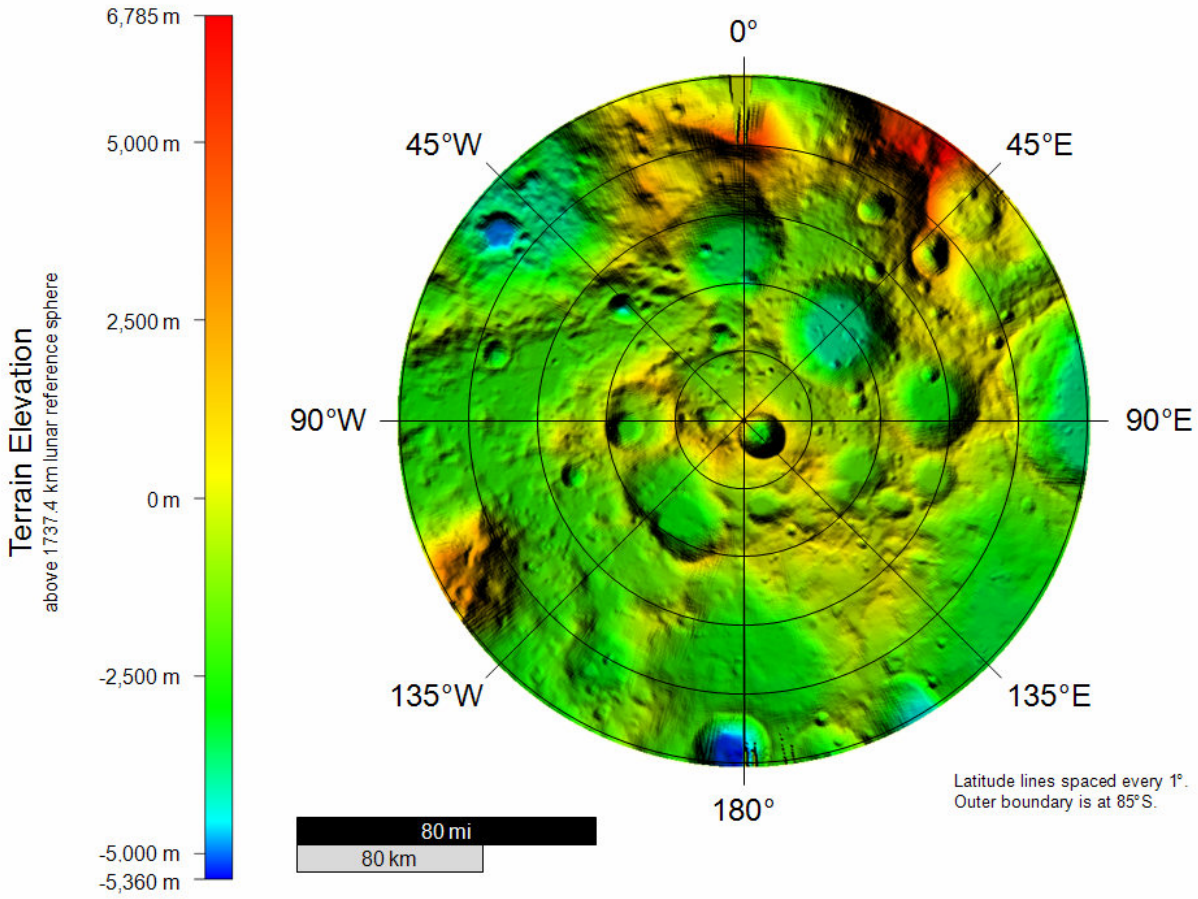

Figure 1. Kaguya (SELENE) terrain data displayed in Global Mapper 10 (adapted for clarity).

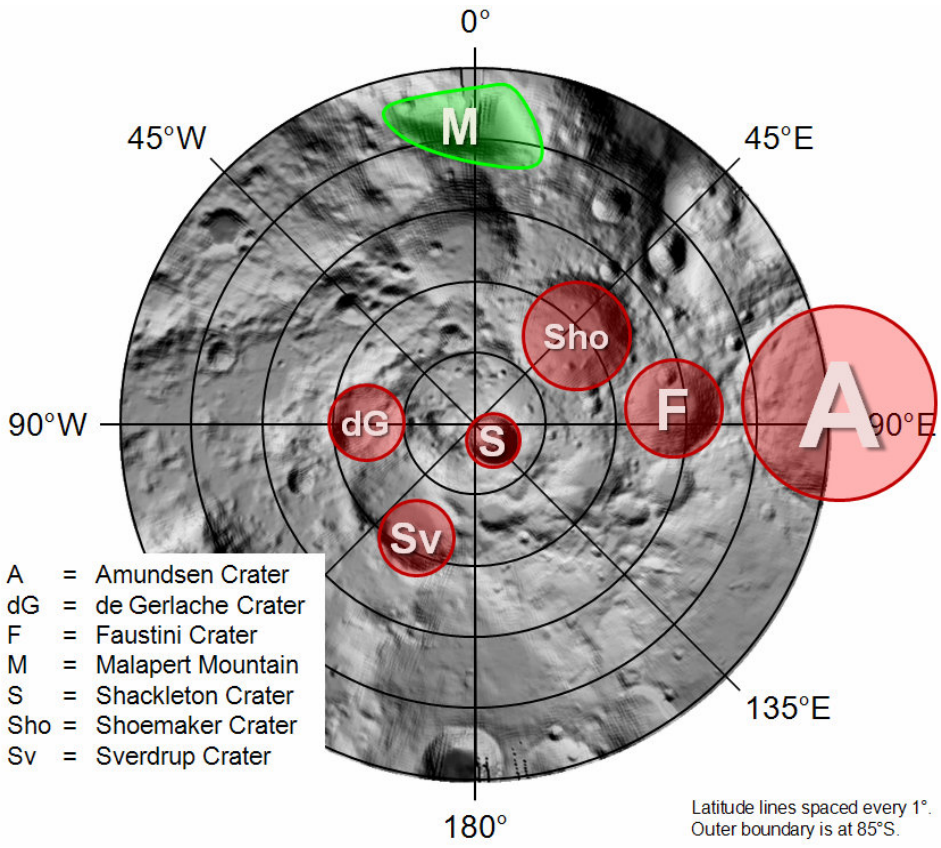

Figure 2. Selected named features in the vicinity of the lunar south pole.[25]

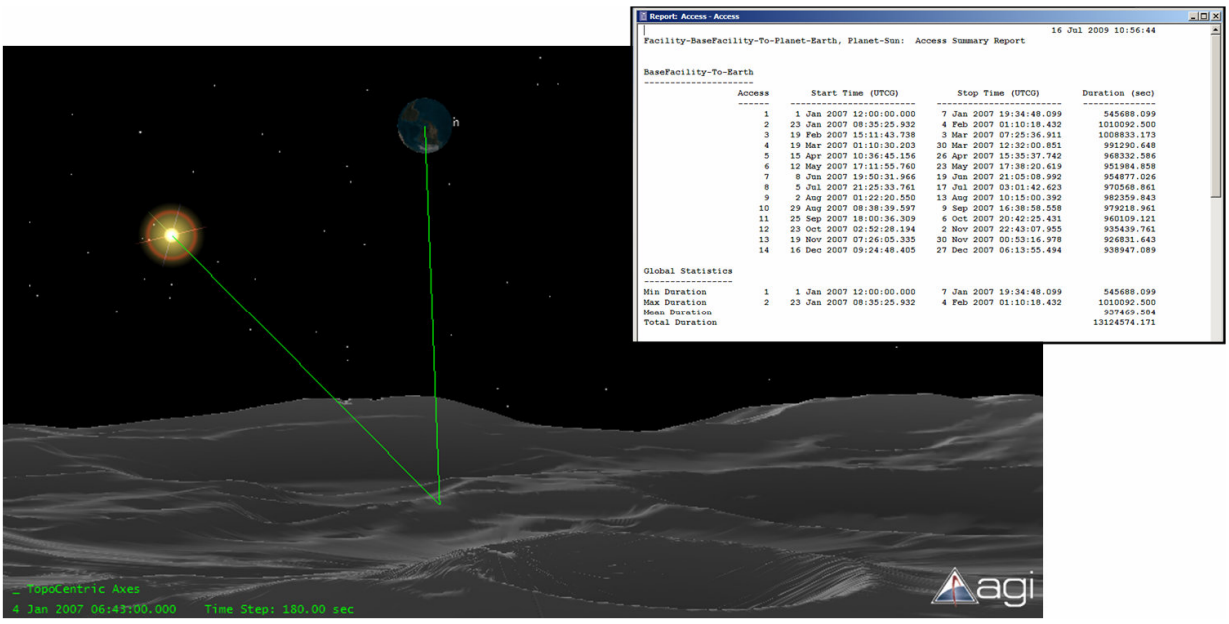

Figure 3. Earth and Sun access lines of sight on Jan. 4, 2007 from 89°S, 0°E, with an STK access report for the year in the upper right corner. Shackleton Crater is in the bottom of the figure, and Malapert Mountain is toward the left, roughly in line with the access lines to Earth and the Sun.

3. Automated MATLAB-STK Analysis

In order to gather Sun and Earth access reports from a wide range of latitude and longitude coordinates rather than a single point, MATLAB is used to interface with STK through the STK Integration toolbox. MATLAB parses through a list of latitude and longitude coordinates, places an STK facility at each coordinate, and records the Earth and Sun access and eclipse periods output by STK. These recorded periods later allow the user to compute statistics such as fraction of time with access, average access duration, and maximum eclipse duration during post-processing. Although the modeled terrain in STK extends as far north as 85°S latitude, access data reported in this paper extends only as far north as 89°S (i.e., in the vicinity of Shackleton Crater; no point in this range is farther than about 30 km from the rim of the crater). As a result, this study draws no conclusions on the viability of a Malapert Mountain landing site (near 86°S, 0°N, which has been proposed in the past[26,27]) except to say that it is very far – approximately 120 km – from Shackleton Crater and an unlikely staging site for physical access to Shackleton.

B. Validation Results

To characterize the fidelity of the STK model, one metric available from this analysis, the illumination rate (or fraction of time for which Sun access is available), is compared to the illumination rate available from the analysis of Ref. 18. Comparison is made for 7,812 regularly-spaced latitude/longitude coordinates at positions south of 89°S. Points within 0.1° in longitude from the anti-meridian and within 0.03° in latitude from the pole are excluded, and it is not recommended that this model be used in those regions. Several differences exist in the assumptions and implementation of these independent analyses, and thus it is not expected that there should be exact agreement. It is also not expected that any one of these differences could account for more than a few percent error. These differences include:

- ***Temporal Discretization.*** While STK computes exact access time periods (reported to fractions of a second), the analysis of Ref. 18 samples access only daily. In Ref. 18, the access condition (i.e., a binary access/no-access response) is sampled at 00:00 UTC on each day of the year; the condition recorded at 00:00 UTC is assumed to hold for the entire day. This would produce discrepancies on [Earth] days when the Sun is visible for only part of the time, but it does not introduce a systematic bias (i.e., it is likely to produce just as many overestimates as underestimates).
- ***Sampling Time Period.*** The validation analysis in STK is run during the year 2007, in particular from 12:00 UTC on January 1, 2007 to 12:00 UTC on January 1, 2008. This allows for all major effects to be captured, i.e., both daily and seasonal variations in sunlight, for a minimum amount of computational time and resources. Ref. 18 performs this analysis over an approximately 5.5-year period starting at 00:000 UTC on January 1, 2000. Because of the unique nature of the precession of the lunar orbital plane and spin axis, the spin axis of the Moon is tilted at an essentially constant 1.6° to the normal to the ecliptic and does not result in substantial lighting variations over the 18.6-year lunar orbit precession cycle (i.e., on the order of 0.5 percent).[18] Thus, error due to this effect is likely to be small.
- ***Angular Size of Sun.*** The STK analysis tracks the line of sight from a point on the lunar surface to the center of the Sun. In reality, the Sun is a finite-size (0.26°) disk in the lunar sky, and Ref. 18 accounts for this, considering illumination to be defined as any time when any part of the Sun's disk is visible. This has the effect of systematically biasing the STK analysis such that it underestimates the amount of illumination with respect to the analysis of Ref. 18. A brief analysis to quantify this has suggested that this error may on the order of 0.5 to 4.0 percent, depending on location and surrounding terrain (e.g., in a 100-day period, the discrepancy between the STK and Ref. 18 analyses due to this effect would be 0.5 - 4.0 days of illumination).
- ***Ephemeris and Moon Orientation.*** The STK analysis uses the default DE405 ephemeris and IAU 2000 lunar orientation and rotation models, while the analysis of Ref. 18 uses DE403 ephemeris and an updated lunar orientation and rotation. While the effect of the ephemeris difference is likely to be negligible, error due to the slightly different lunar orientation may be noticeable, particularly at polar locations. Future analyses aim to quantify this effect.
- ***Terrain Elevation Offset.*** As mentioned in Section II.A.1, the terrain model in STK is elevated +10 km from the actual Kaguya (SELENE) elevation to overcome a modeling limitation at the anti-

meridian. Because the driver of illumination rate is the elevation angle of the Sun and its interaction with local terrain elevation, terrain orientation is paramount. A 10 km translational discrepancy is unlikely to have a major effect on terrain orientation with respect to the Sun since the distance between the Moon and Sun is seven orders of magnitude larger, at 1.5×10^8 km.

- ***Computational Algorithms.*** The analysis of Ref. 18 used a custom computer code, which may introduce additional discrepancies when compared to the proprietary STK code. For example, differences in terrain interpolation methods are not well understood. These discrepancies, however, are difficult to quantify without an additional dedicated analysis.

The illumination maps used in the validation study are shown in Fig. 4. The data in the map on the left were provided by the authors of Ref. 18 at the National Astronomical Observatory of Japan (NAOJ), and the map on the right was generated using the STK model generated for this study. It is visually clear that the two match quite well. Shackleton Crater is the most obvious feature in each plot, filling most of the lower right quadrant of the map with a circular area with zero percent illumination. The outside walls of Shackleton have moderate amounts of illumination (around 40%), and the upper left quadrant is largely devoid of illumination because of shadowing from distant mountains as well as the rims of nearby Shackleton and de Gerlache craters. The lower left quadrant, which contains a ridge connecting the rims of Shackleton and de Gerlache, is an area with an illumination rate as high as 76.2% (STK prediction) or 75.5% (NAOJ prediction).[‡]

Figure 5 shows the subtraction of the NAOJ prediction from the STK prediction (i.e., from Fig. 4, the right plot minus the left plot). The plot on the left in Fig. 5 shows the spatial distribution of illumination rate errors, where the colors yellow, orange, and red indicate that the STK model overpredicts illumination and the color blue indicates that the STK model underpredicts illumination relative to the NAOJ model. Note that the majority of the map is colored green (essentially zero error) or light blue (a slight underprediction).

Also informative are the histograms of the error shown on the right in Fig. 5, which display the information statistically. The upper histogram shows that the vast majority of errors are between -0.1 and +0.1, with a slight bias downward (i.e., toward STK underpredicting illumination). The mean (-0.0178) and median (-0.0139) confirm this; the central tendency of the STK model is to underpredict illumination by 1.4 to 1.8 percentage points compared to the NAOJ model. The lower histogram shows the distribution of the absolute value of the error, allowing statements to be made about the likelihood of a randomly selected STK prediction differing from the NAOJ model by a certain amount. The lower histogram shows that the 90th percentile error is 0.0749 (i.e., 90% of the time, a randomly selected data illumination rate will be in error by 7.5 percentage points or less). The 95th percentile error is 0.0991, and the 99th percentile error is 0.1482.

While this error is considered suitable for the purposes of this study and the use of the model in conceptual design, future studies and model development may seek to reduce this discrepancy between the data sets. The first assumptions to investigate in depth are the differences listed earlier. It is worth noting that the error in the upper histogram appears to be essentially normally distributed, a behavior that might be expected for factors mentioned earlier that had no clear systematic biasing effect (such as time discretization). Interestingly, the major biasing effect recognized earlier was the consideration of the Sun as a disk rather than a point, which was roughly estimated to bias the STK model to underpredict illumination on the order of 0.5 to 4.0 percent. This is consistent with the 1.4 to 1.8 percent underprediction central tendency seen here.

[‡] Note that this is only the maximum seen from the 7,812 points used in the validation.

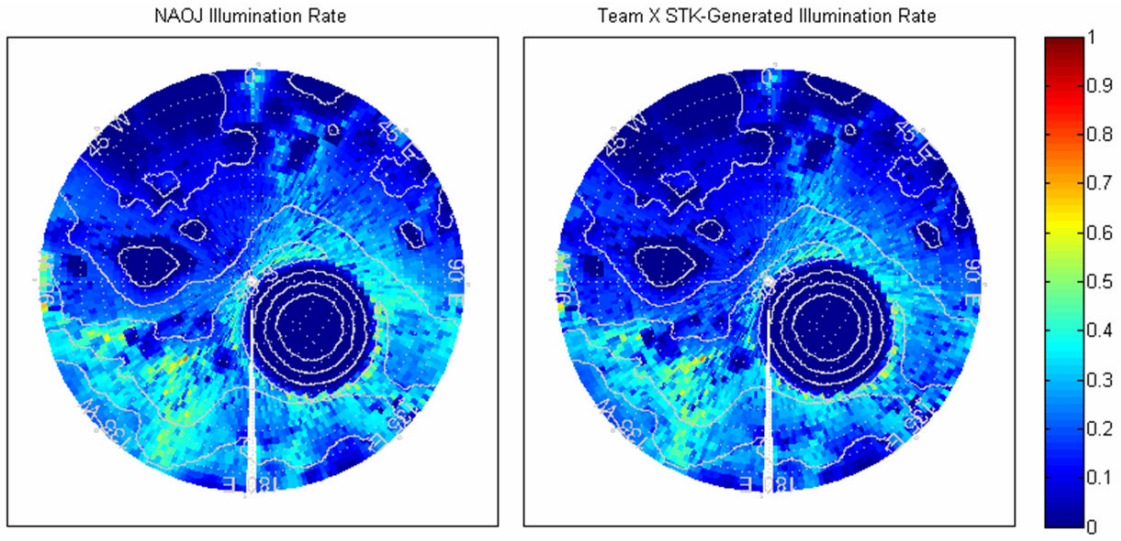

Figure 4. Maps of illumination rate (fraction of time with Sun access) for the 7,812 validation points as a function of latitude and longitude. *Data from Ref. 18, by the National Astronomical Observatory of Japan (NAOJ), is on the left. Data from the STK model used in this paper is on the right. The northern extent of the map is 89°S, and contours indicate 1 km changes in terrain elevation.*

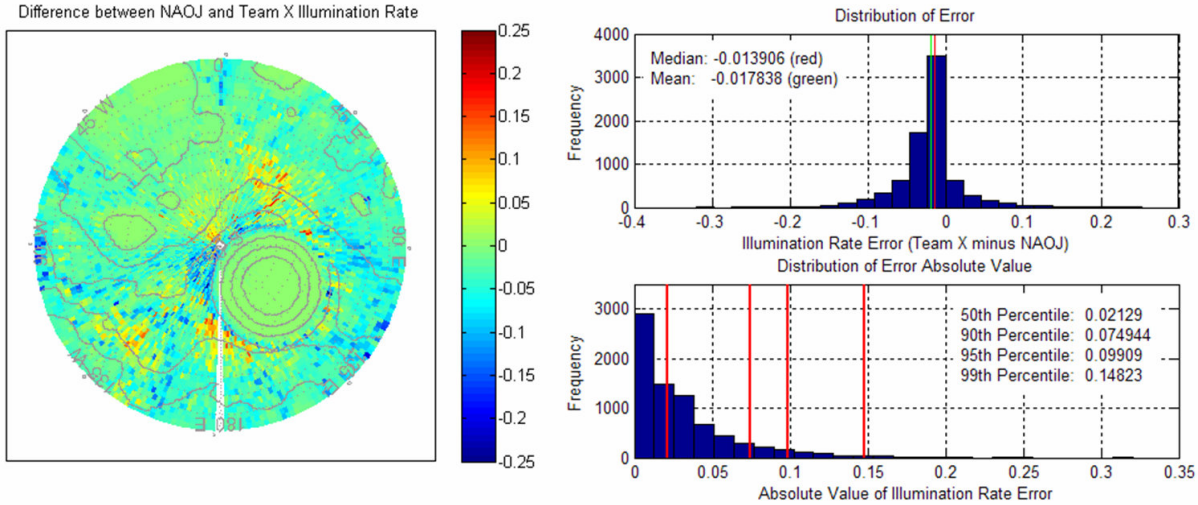

Figure 5. Statistics on the arithmetic difference between the illumination rate predicted by model used in this paper and the data of Ref. 18 (i.e., statistics on the subtraction of the two plots in Fig. 4, as STK prediction minus Ref. 18 prediction). *The plot on the left indicates the spatial distribution of errors (red indicates STK overpredicting the amount of illumination, and blue indicates an underprediction relative to Ref. 18). The two histograms on the right indicate the statistical distribution of the error. The northern extent of the map is 89°S, and contours indicate 1 km changes in terrain elevation.*

III. Results and Discussion

A. Scenarios Studied

The results that follow utilize the STK model described in Section II, and Sun and Earth access conditions for three parametric variations, shown in Table 1, have been generated to account for three scenarios of interest. The three scenarios are designed to capture differences in access due to the effect of the altitude at which access is tracked.[§] This effect is relevant from an operational perspective. For example, access exactly at the surface of the Moon is relevant when computing surface temperatures and identifying regolith in permanent darkness, and this metric is frequently the only one considered in illumination rate studies. However, access at 1 m above the surface is more relevant for robotic mission scenarios, where solar arrays or Earth-pointing antennas will be somewhat elevated from the surface. Access at 10 m above the surface is more relevant for large human-class spacecraft. In combination, these three sets can also be used to interpolate if a given spacecraft configuration does not precisely match the 0, 1, or 10 m altitudes.

As shown in Table 1, Set #1, the baseline condition, is surface access during the year 2011. Set #1 contains 32,384 data points spaced at latitude intervals of 0.0156° (473.8 m) and longitude intervals of 0.7115° (376.5 m at the -89°S edge of the analysis area). Sets #2 and 3 are identical to Set #1 except that the altitude of the facility created in STK is raised by 1 and 10 m, respectively.

Table 1. Three Scenarios Analyzed.

Set No.	Scenario	Altitude	Year	Data Points
1	Baseline: Surface Access	0 m	2011	32,384
2	Notional Robotic System Access	1 m	2011	32,384
3	Notional Human System Access	10 m	2011	32,384

B. Set #1: Baseline Results

Presented here are results from Set #1, the baseline case described above. Access is tracked at the surface (0 m altitude) during the year 2011. Covered first are maps of the traditional access rates (fraction of time with access) as well as maps of maximum eclipse durations. Next, a site selection and decision tool is introduced and used to combine multiple measures of site suitability into a map of overall suitability. This allows for selection of optimal sites and regions given user weights and constraints. Following this is an identification of Pareto-optimal sites, independent of user weights.

1. Access and Eclipse Metric Maps

Figure 6 shows the fraction of time that the Sun and Earth are accessible during the year 2011. Shackleton Crater is clear in both maps, as are other depressions that prevent visibility to both Sun and Earth. However, the similarities in the plots essentially end there. Earth access is bimodally distributed across the map; large portions of the map have high Earth access (the highest is 58.3%, near the southern rim of de Gerlache at 89.0234°S, 92.4012°W), and other large portions have virtually no access. Few points fall between these extremes, and this is caused by the fact that the Moon is tidally locked in its orbit around Earth. In contrast, the Sun clocks around the south polar region once per lunar day, and Sun access is more evenly distributed. The maximum Sun access detected is 77.0%, near the southeastern extent of Shackleton at 89.7733°S, 155.7213°W. However, another region of high Sun access is the ridge connecting Shackleton and de Gerlache, particularly near 89.4°S, 135°W.

Figure 7 shows the maximum duration of no-access, or eclipse, periods for the Sun and Earth. This is of significance to power system and telecommunications design because even if a site's accessible fraction of time is

[§] Consideration was given to also parametrically varying the sampling year, but the ranges of Sun and Earth elevation angles above the lunar south pole horizon do not exhibit long-term trends when plotted over a period of several years. That is, the Sun and Earth rise just as high above the lunar south pole horizon in 2011 as they do in 2006 (a year of maximum Earth-relative inclination) or 2015 (a year of minimum Earth-relative inclination). As a result, the sampling year should have a minimal effect on Sun and Earth access. The year assumed for all results shown here is 2011, approximately in the middle of the 18.6-year lunar orbit precession cycle when the Moon is at an Earth-relative inclination of 23.5°.

high, terrain or seasonal effects may cause large periods of time with no access. Note that in Fig. 7, the upper limit on the color axis is 90 days, and any eclipse times greater than 90 days are maroon in color. As might be expected due to the fact that the Earth occupies a very small, consistent portion of the lunar sky, the map of Earth maximum eclipse duration is closely correlated with its counterpart in Fig. 6. Its bimodality in color, in combination with the access data in Fig. 6, indicates that if a site has Earth access at all, then the maximum eclipse can be generally expected to last 13-14 days. On the Sun maximum eclipse duration map, a dramatic transition to long eclipses can be seen in the upper half of the map. These long eclipses occur as the Sun sets behind local terrain during the lunar winter, and this information is not captured in Fig. 6. Interestingly, since the reduction in Earth eclipse duration favors the upper half of the map and reduction in Sun eclipse duration favors the lower half, this suggests a compromise may be required in landing or outpost site selection. This type of compromise and the consideration of multiple objectives in selecting a landing site drives the analysis detailed next.

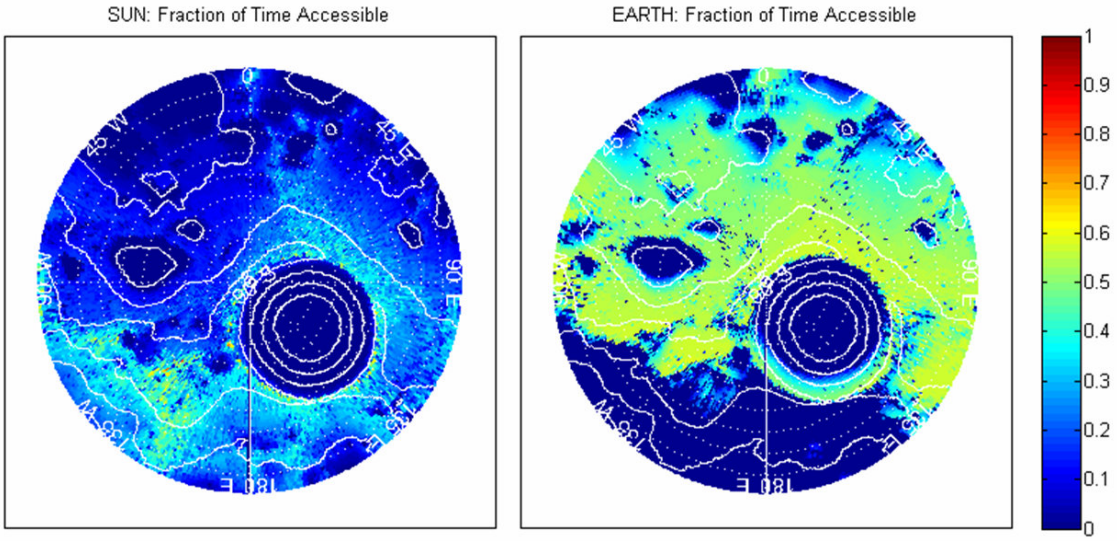

Figure 6. Maps of fraction of time with Sun access (left) and Earth access (right) for Set #1.
The northern extent of the map is 89°S, and contours indicate 1 km changes in terrain elevation.

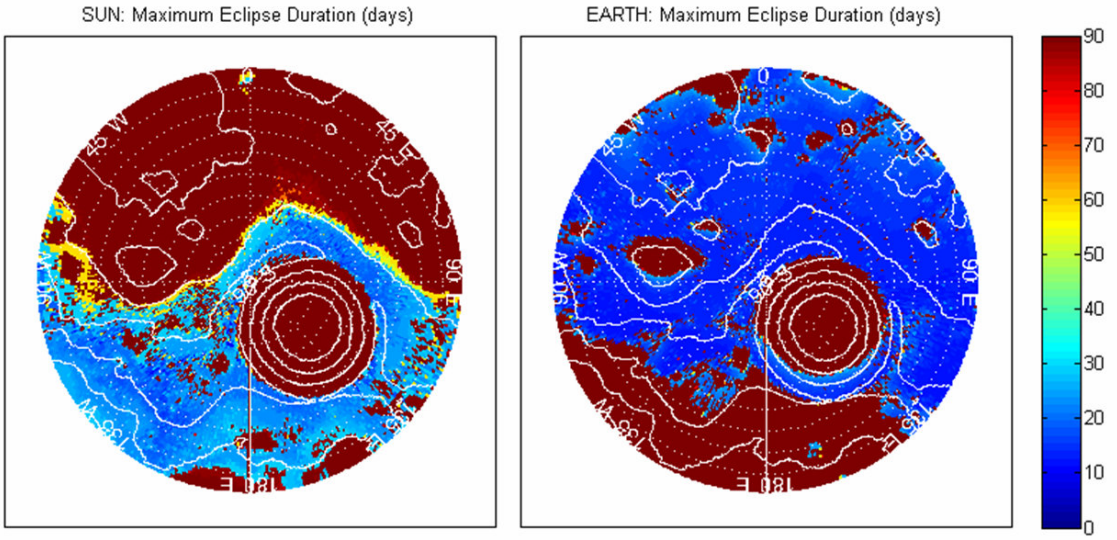

Figure 7. Maps of maximum time without Sun access (left) and Earth access (right) for Set #1.
The northern extent of the map is 89°S, and contours indicate 1 km changes in terrain elevation.

2. Decision Tool and Optimal Site Selection

The analysis described above produces a variety of Sun and Earth access statistics for each point on the lunar south pole map. Given the quantity of data generated at each of the 32,384 points, it can be difficult to identify the optimum landing site by inspection of these maps. This is especially true since the statistics represented on each map vary in importance with the mission scenario. This section illustrates a method by which multiple metrics of interest can be combined into a single suitability metric, permitting more straightforward selection of a single landing or outpost site.

Figure 8 shows a graphical user interface (GUI) decision-making tool that allows a user to interactively set relative weights and filters for key parameters of interest in order to identify highly-desirable locations. In the upper left of the GUI, the user inputs relative weights for each of six metrics: Percent Sun Access, Percent Earth Access, Maximum Sun Eclipse Duration, Maximum Earth Eclipse Duration, Sun Eclipse Duration Standard Deviation, and Earth Eclipse Duration Standard Deviation. The first four metrics are identical to those demonstrated in Section III.B.1, and the last two are measures of the consistency of eclipse periods. Collectively, these metrics represent the desire for a site to have (1) a large amount of time with access to the Sun or Earth, (2) short worst-case Sun and Earth eclipse periods, and (3) eclipse period durations that are regular. While these three desires are correlated, they represent important and conceptually distinct objectives. The weights indicated by the slider bars and numbers indicate the relative importance of each metric to the user; for example in Fig. 8, the most important metric to the user is the maximum duration for which the Sun is not accessible. The weights in Fig. 8 were determined through a pairwise-comparison-based Analytic Hierarchy Process (AHP),[28] and they clearly favor Sun access over Earth access, representative of a solar-powered spacecraft with access to a relay satellite for Earth communication. However, these weights can be easily and interactively modified by the user to reflect different mission scenarios.

On the right in the GUI are filters associated with each of the six metrics of interest. Here, the user may set thresholds for which data is displayed. For example, if the user wishes to consider only locations with Sun access more than 50% of the year, the "Percent Sun Access" filter may be set to 50%, and no locations with less than 50% Sun access will be displayed on the resulting map, nor will they be scored for the optimization process.

Once weights and filters are set, the user may click the "Update Map" button to perform the optimization analysis and display a color map of site suitability. The map resulting from the user's preferences in Fig. 8 is shown on the left plot of Fig. 9. The score displayed in terms of color is computed using the Technique for Order Preference by Similarity to Ideal Solution (TOPSIS), which determines a point's score based on its euclidean closeness to the positive ideal (utopia) point of the data set and its euclidean distance from the negative ideal (anti-utopia) point of the data set.[29] High scores (i.e., highly desirable sites) are represented in red. Areas that have been omitted due to filter settings are represented in white. In the left plot of Fig. 9, no filter settings are active, and every location has a score and color associated with it. Some maroon, very-high-score regions are evident along the ridge connecting Shackleton and de Gerlache craters. Note that the craters themselves have appreciable scores because only one eclipse period exists (the 365-day eclipse for the entire analysis time period) and as a result they have very small eclipse duration standard deviations. In the plot on the right in Fig. 9, filter settings have been imposed such that the only points shown are those with more than 0% Sun and Earth access and less than 90 days of maximum Sun and Earth eclipse duration. As a result, the feasible area is considerably smaller than in the left plot, limited primarily to the rim of Shackleton Crater, the western outer slope of Shackleton, and the ridge connecting Shackleton and de Gerlache.

After a user clicks "Update Map" in the Fig. 8 GUI, the coordinates of the optimum (highest-scoring) site are displayed toward the bottom left of the GUI. The user has the option of clicking "Query this Point" to see detailed statistics about the site. The query results for the optimum site for the Fig. 8 GUI are shown in Fig. 10. This site is on the southwestern rim of Shackleton Crater (see the yellow star in the right plot of Fig. 9) and has Sun access 77.0% of the year (the highest value on the map) and Earth access 57.2% of the year. The maximum duration during which the Sun is not accessible is 6.1 days, the lowest over the entire map, and access during the lunar south pole summer is uninterrupted for a period of 117.2 days (nearly four months). Earth access periods are regularly 15-16 days in duration, and Earth eclipse periods are regularly 11-12 days in duration. Figure 11 shows STK visualizations of this location.

In addition to the ability to query the optimal point, the GUI also allows the user to either point and click or manually input coordinates to query any point on the map (after clicking the "Query Point on Map" button). Additionally, the user may place a yellow star marker at the current point on the map by clicking the "Show on Map" button in the GUI.

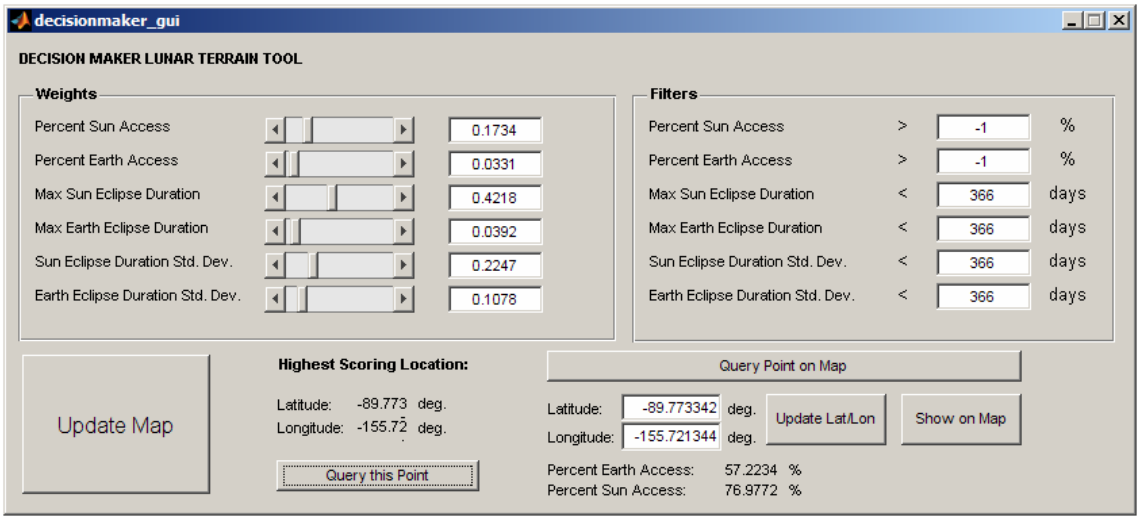

Figure 8. Decision-Maker Graphical User Interface.
The weights set in this example are determined via AHP, and filters are effectively deactivated.

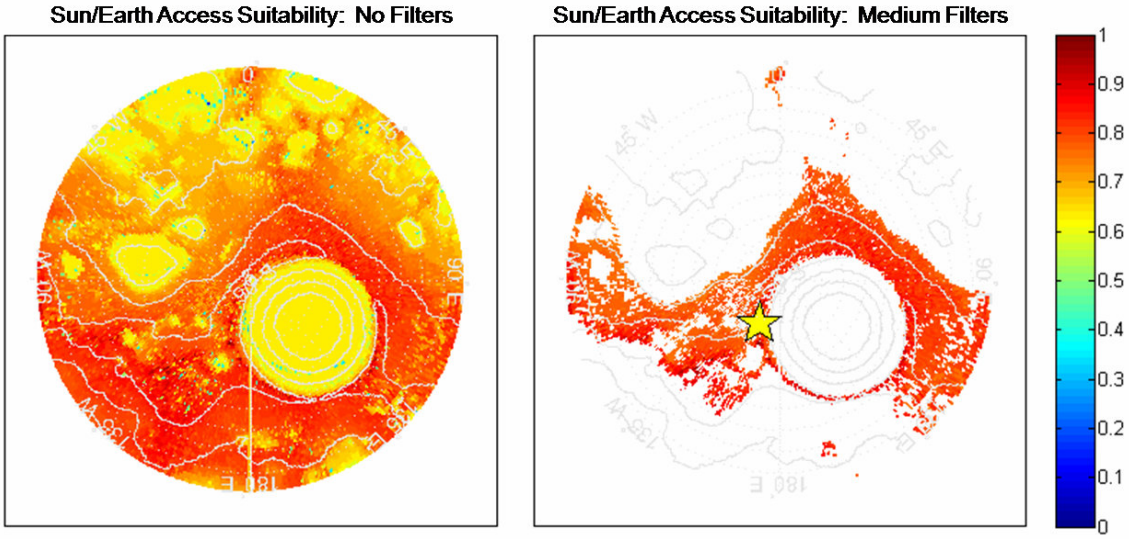

Figure 9. Maps of site suitability with no filters (left) and with moderate/medium filters (right).
The yellow star in the right plot indicates the optimum site for the selected objective weights. The northern extent of the map is 89°S, and contours indicate 1 km changes in terrain elevation.

Optimal Location Results
AHP Weighting Scheme

89.7733°S, 155.7213°W

57.2% Earth Access
77.0% Sun Access

Max Earth Eclipse: 12.7 days
Max Sun Eclipse: 6.1 days

Max Earth Access: 16.1 days
Max Sun Access: 117.2 days

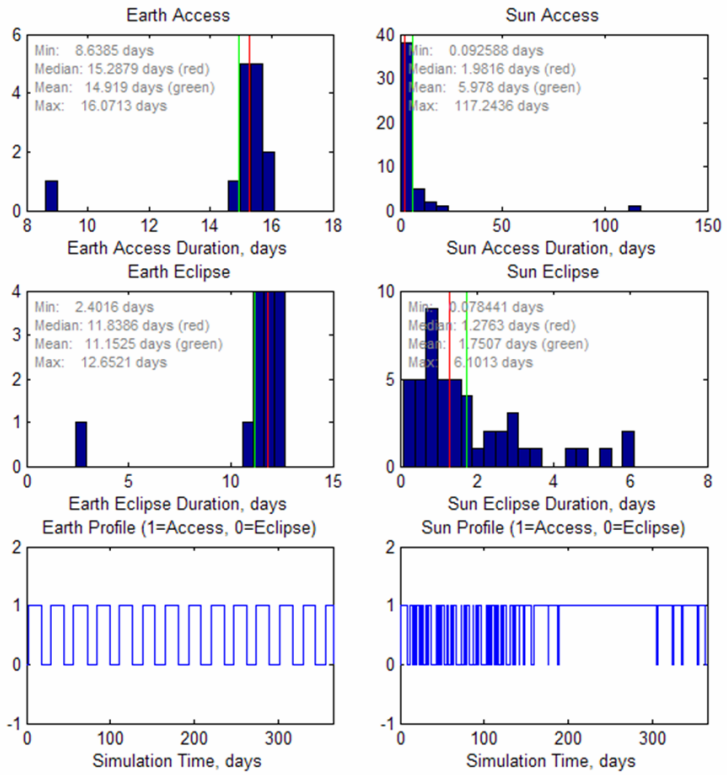

Figure 10. Detailed statistics on Earth and Sun access for the optimal location according to the Fig. 8 weights.
The top plots are histograms of Earth and Sun access durations, the middle plots are histograms of Earth and Sun eclipse durations, and the bottom plots show simulation time histories of Earth and Sun access.

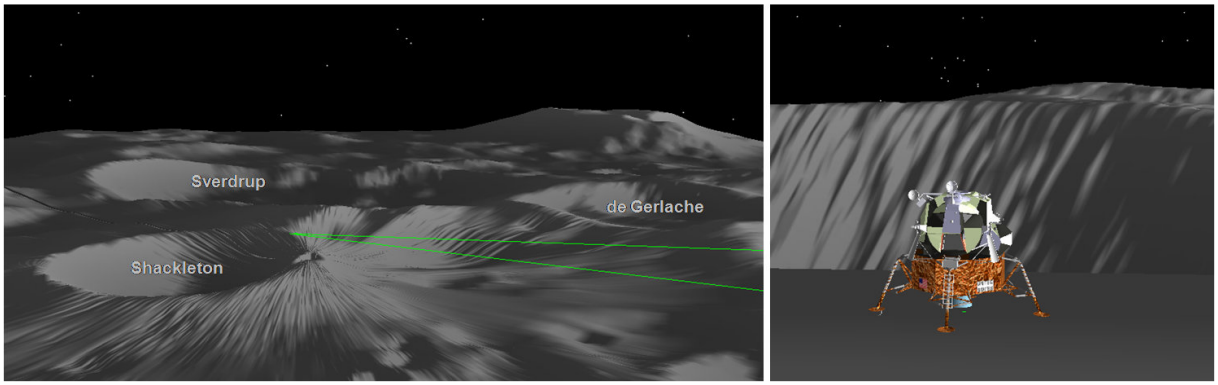

Figure 11. STK visualizations of the optimal location according to the Fig. 8 weights.
In the left illustration, the site is on the rim of Shackleton at the intersection of the two green Sun and Earth access lines. The right illustration shows an Apollo Lunar Module landed at the optimal location, overlooking Shackleton.

As mentioned earlier, the optimal point identified by the decision tool depends on the weights a user inputs. These inputs may depend significantly on the mission scenario. For example, if an early robotic mission to the Moon is to be powered by a radioisotope thermoelectric generator (RTG), the requirement for Sun access may be greatly reduced or eliminated while Earth access may still be critical (e.g., if a communications relay satellite is not yet in place). A notional weighting scheme for such a mission is input to the GUI in Fig. 12. The new weights result in the suitability map in Fig. 13, which differs significantly from Fig. 9.

The optimum site according to the new weights is located on the ridge between Shackleton and de Gerlache craters (see the yellow star in Fig. 13). As given by Fig. 14, this site has Sun access 70.1% of the year (6.9% less than the previous optimum) and Earth access 58.1% of the year (0.9% more than the previous optimum). The maximum duration during which the Sun is not accessible is 11.5 days, and the maximum access duration is 26.4 days during the lunar south pole summer. Because of the emphasis on Earth access regularity in the weighting scheme, Earth access periods are regularly 15.7 days with very little variation, and the intervening eclipse periods are regularly 11.5 days long. Figure 15 shows STK visualizations of this location.

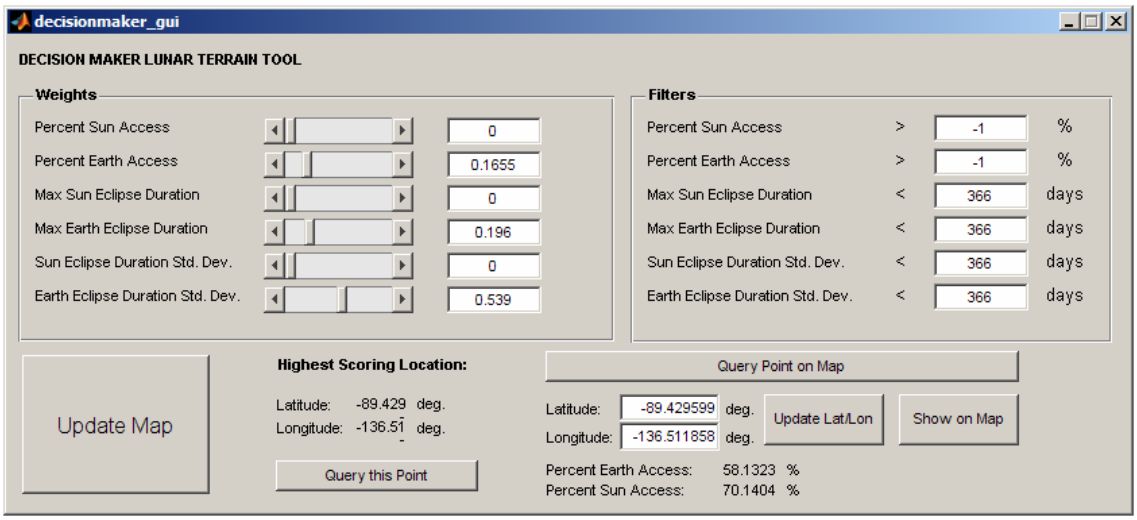

Figure 12. Decision-Maker Graphical User Interface for a Notional RTG-Powered Mission. *This scenario has virtually no need for solar power and emphasizes consistent, short-eclipse Earth access. Filters are deactivated.*

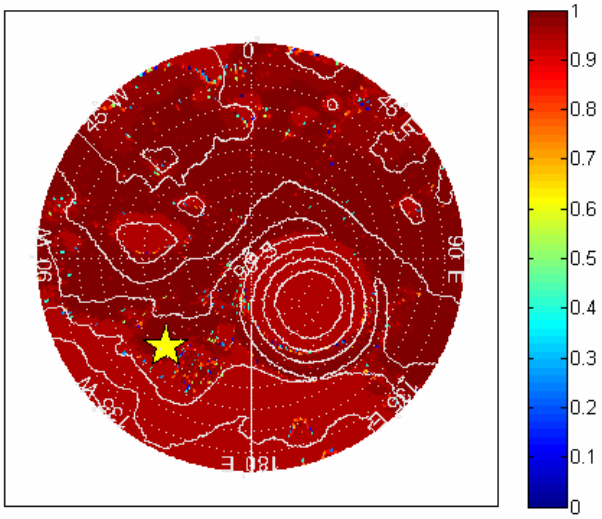

Figure 13. Map of site suitability with no filters, using the weights in Fig. 12.
The yellow star indicates the optimum site for the selected weights. The northern extent of the map is 89°S, and contours indicate 1 km changes in terrain elevation.

Optimal Location Results
Notional RTG Weightings

89.4296°S, 136.5119°W

58.1% Earth Access
70.1% Sun Access

Max Earth Eclipse:	12.1 days
Max Sun Eclipse:	11.5 days
Max Earth Access:	15.8 days
Max Sun Access:	26.4 days

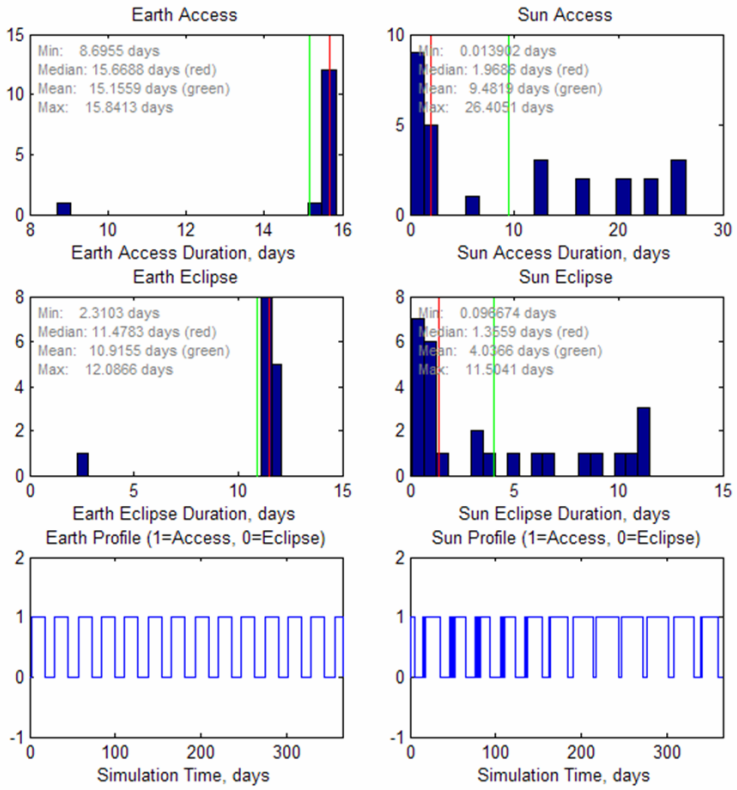

Figure 14. Detailed statistics on Earth and Sun access for the optimal location according to Fig. 12 weights.
The top plots are histograms of Earth and Sun access durations, the middle plots are histograms of Earth and Sun eclipse durations, and the bottom plots show simulation time histories of Earth and Sun access.

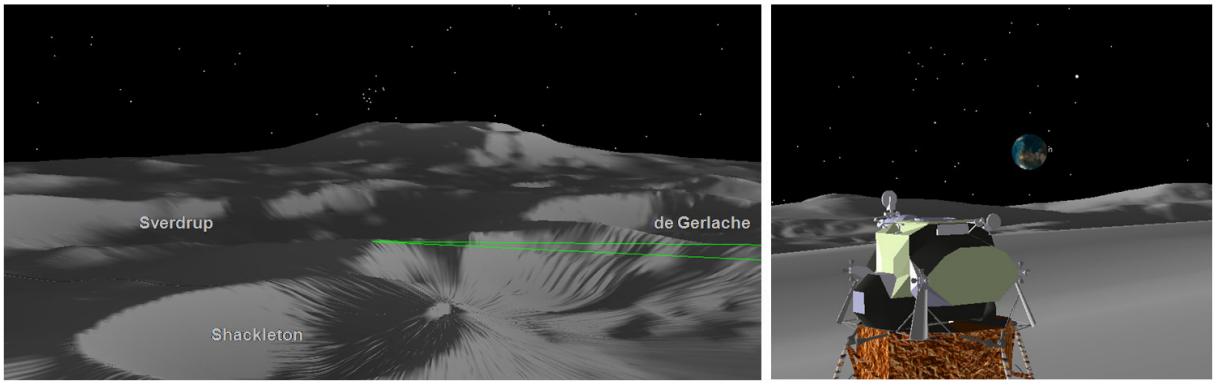

Figure 15. STK visualizations of the optimal location according to the Fig. 12 weights.
In the left illustration, the site is on the ridge between Shackleton and de Gerlache at the intersection of the two green access lines. The right illustration shows an Apollo Lunar Module landed at the optimal location.

3. Pareto-Optimal Sites

A natural follow-on question after the previous analysis involving subjective weighting schemes is whether it is possible to identify sites that would be optimum no matter what weighting scheme is chosen. This leads to the notion of Pareto optimality. A Pareto-optimal point is one that is non-dominated, or one for which no points exist that are more desirable in every category. The set of Pareto-optimal points in an objective space is known as a Pareto front or Pareto frontier. These points are the only points relevant for trade studies, provided that all objectives have been accounted for in the metrics of interest. For this analysis, it is assumed that all objectives except for the six weighted in the GUI are negligible.[**]

To generate the set of Pareto-optimal points, each of the 32,384 data points in the set is compared to each other data point to determine whether any is equal or superior to the current point in all six objective dimensions. This reduces the list of potential data points from 32,384 to just 28 points. These 28 points are theoretically the only points that should be considered when examining trades among the six defined objectives. These points and their performance with respect to the six objectives are listed in Table 2.

The first 19 points in Table 2 are of greatest interest. Note that Point #4 near de Gerlache has the highest percent access to Earth and the minimum longest Earth eclipse period. Point #16 is the same point that was identified in the alternate weighting scheme for the notional RTG-powered early robotic mission, and it has the smallest nonzero standard deviation in Earth eclipse duration. Point #19 is the same point that was identified in the initial AHP-based weighting scheme, and it scores highest[††] in terms of all three Sun access metrics. As a result, if only Sun access were considered, Point #19 would always appear as the undisputed best point on the map. Points #20-28 are technically Pareto-optimal because they have the best possible (zero) standard deviation for Sun or Earth eclipse duration. However, these points are not of practical interest because the zero eclipse duration standard deviation is due to the fact that a single 365-day eclipse exists (i.e., the sites are in permanent eclipse, with no access to either Earth or the Sun).

Interestingly, Points #1-19 are clustered in four distinct geographic areas, mapped in Fig. 16. All are in the western hemisphere. The northernmost region is close to the edge of de Gerlache Crater, at the northern edge of the map. Moving southwest about 15 km between de Gerlache and Shackleton, a distinct 6 km long line of Pareto-optimal points exists along a ridgeline running south. Moving west from here by another 9 km, another series of Pareto-optimal points exists along a second ridgeline. This second ridgeline is about 11 km from Point #19 on the rim of Shackleton Crater. This clustering of points suggests that the locations of the three major clusters (on de Gerlache and the two ridgelines) are areas that will consistently stand out regardless of the weights a user assigns to the six objectives. It is worth noting that, perhaps surprisingly, the rim of Shackleton Crater has only one Pareto-optimal point (Point #19). Figures 17 and 18 provide birds-eye 3-D views of the nineteen Pareto-optimal locations of interest using the STK visualization capability.

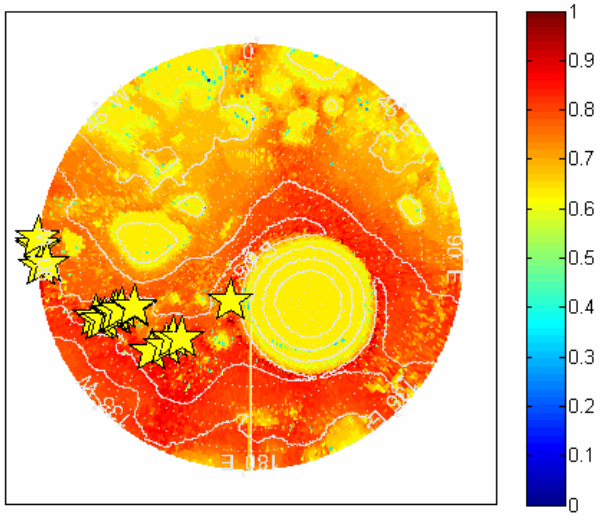

Figure 16. Pareto-optimal points (yellow stars) overlaid on the left plot from Fig. 9. *The northern extent of the map is 89°S, and contours indicate 1 km changes in terrain elevation.*

[**] Future analyses may prefer to add objectives, such as surface slope and roughness, as well as distance to the nearest point of interest. This can be easily accommodated in the future.

[††] Strictly speaking, this point actually has a Sun eclipse standard deviation inferior to Points #20-22, which have zero standard deviation because they are in permanent Sun eclipse. More correctly, Point #19 has the best nonzero Sun eclipse duration standard deviation.

Table 2. Pareto-Optimal Points for Baseline Surface Access.

Point No.	Latitude	Longitude	Percent Access		Max Eclipse (d)		Ecl. STDV (d)		Comments
			Sun	Earth	Sun	Earth	Sun	Earth	
1	89.0077°S	87.4209°W	48.3%	57.7%	16.12	11.92	5.07	2.62	
2	89.0077°S	86.7095°W	48.6%	57.7%	16.40	11.96	4.95	2.62	
3	89.0077°S	84.5751°W	50.1%	57.6%	15.47	11.99	4.50	2.62	
4	89.0234°S	92.4012°W	47.7%	58.3%	16.51	11.71	5.03	2.59	Max Earth Access Pct, Shortest Max Earth Eclipse
5	89.0546°S	91.6897°W	32.9%	57.9%	15.24	11.79	5.13	2.60	
6	89.2265°S	110.8992°W	57.8%	57.0%	14.97	12.00	4.70	2.56	
7	89.2421°S	113.0336°W	51.4%	57.2%	13.90	11.96	5.69	2.55	
8	89.2577°S	113.0336°W	52.2%	57.2%	16.41	11.93	5.95	2.53	
9	89.3046°S	112.3221°W	42.9%	57.3%	14.95	11.93	6.35	2.52	
10	89.3202°S	113.7451°W	63.2%	57.5%	18.59	11.90	5.15	2.51	
11	89.3202°S	112.3221°W	48.7%	57.4%	15.05	11.92	5.29	2.51	
12	89.3515°S	112.3221°W	50.0%	57.4%	8.02	11.93	2.64	2.50	
13	89.3671°S	133.6660°W	62.8%	57.6%	10.95	12.16	4.23	2.50	
14	89.4140°S	113.7451°W	36.6%	57.3%	26.68	12.03	8.16	2.50	
15	89.4140°S	113.0336°W	24.1%	57.3%	25.81	12.05	10.10	2.50	
16	89.4296°S	136.5119°W	70.1%	58.1%	11.50	12.09	4.17	2.49	Min Nonzero Earth Ecl. STDV, Opt. in Figs.12-15
17	89.4765°S	136.5119°W	72.4%	58.1%	11.85	12.12	3.32	2.49	
18	89.5077°S	140.0692°W	76.8%	57.8%	9.47	12.17	2.67	2.50	
19	89.7733°S	155.7213°W	77.0%	57.2%	6.10	12.65	1.51	2.56	Nonzero Best for All Sun Metrics, Opt. in Figs. 8-11
20	89.1640°S	26.9466°W	0.0%	43.4%	365.00	15.78	0.00	3.13	Permanent Sun Eclipse
21	89.2421°S	75.5040°E	0.0%	43.5%	365.00	15.80	0.00	3.11	Permanent Sun Eclipse
22	89.8202°S	39.7530°W	0.0%	43.7%	365.00	15.84	0.00	3.08	Permanent Sun Eclipse
23	89.3046°S	145.0494°W	59.0%	0.0%	14.27	365.00	3.55	0.00	Permanent Earth Eclipse
24	89.3046°S	142.9150°W	48.7%	0.0%	16.68	365.00	3.45	0.00	Permanent Earth Eclipse
25	89.3046°S	139.3577°W	49.3%	0.0%	16.85	365.00	3.52	0.00	Permanent Earth Eclipse
26	89.3202°S	142.9150°W	61.8%	0.0%	14.81	365.00	3.71	0.00	Permanent Earth Eclipse
27	89.3515°S	142.2036°W	59.8%	0.0%	14.48	365.00	5.00	0.00	Permanent Earth Eclipse
28	89.9608°S	63.9427°W	9.6%	0.0%	27.56	365.00	3.17	0.00	Permanent Earth Eclipse

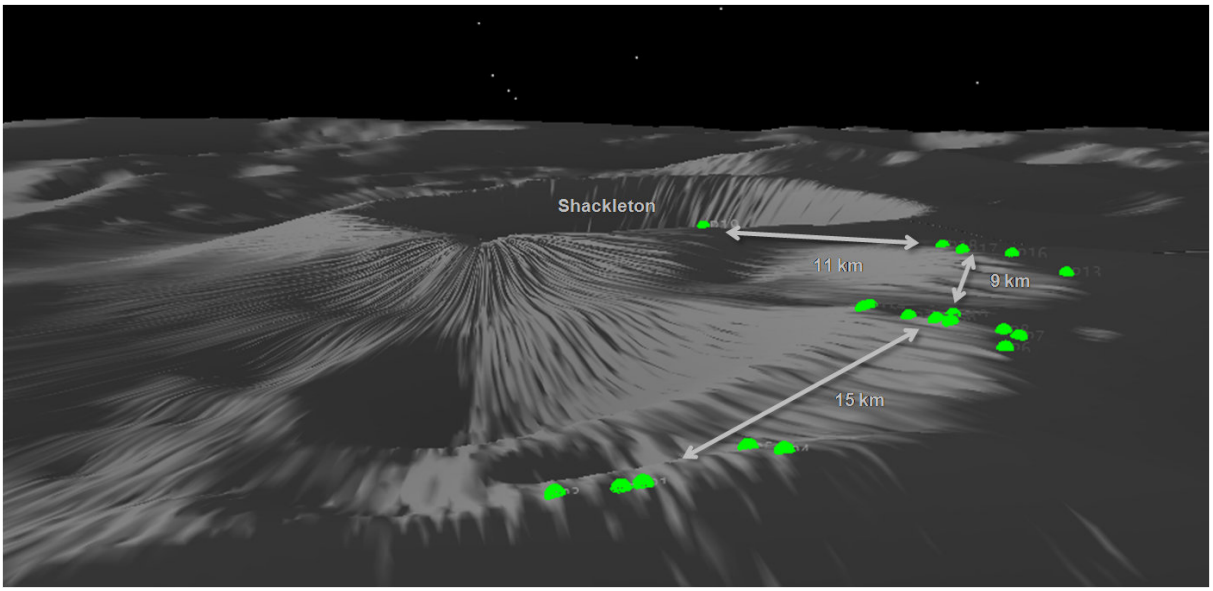

Figure 17. STK visualization of Pareto-optimal locations for the Baseline Surface Access condition.
The camera in this image is positioned above de Gerlache Crater. Points #20-28 are excluded.

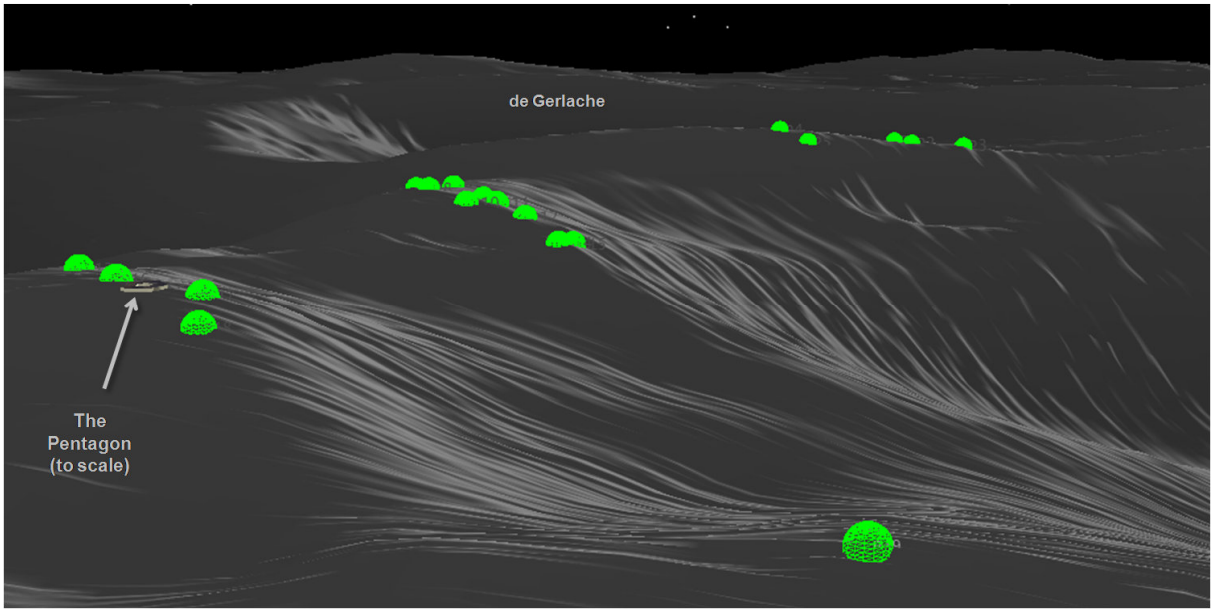

Figure 18. STK visualization of the Pareto-optimal locations for the Baseline Surface Access condition.
The camera in this image is positioned above Shackleton Crater. Points #20-28 are excluded.

C. Set #2: +1 m Notional Robotic Mission Results

Presented here are results from Set #2, the analysis set that considers access as assessed one meter above the lunar surface. This is intended to be realistic for antenna or solar array placement conditions for robotic missions, and tracking access at this slightly elevated altitude mitigates the effects of any small but sharp terrain features that could obstruct viewing locally. As with Set #1, covered first are maps of the traditional access rates (fraction of time with access) as well as maps of maximum eclipse durations. Next, the site selection and decision tool is used to determine an optimal site for a given set of user weights. Following this is an identification of Pareto-optimal sites for this scenario.

1. Access and Eclipse Metric Maps

Figure 19 shows the fraction of time that the Sun and Earth are accessible at the +1 m altitude. Just as with the surface data shown in Fig. 6, Shackleton Crater is clear in both maps, as are other depressions that prevent visibility to both Sun and Earth. Earth access is again bimodally distributed across the map, with large portions of the map having high Earth access and others having virtually no access. There is no substantial change in the optimum Earth access condition with the raised altitude: The highest Earth access percentage is again 58.3%, located at the same location on the rim of de Gerlache at 89.0234°S, 92.4012°W. However, note that in the right plot of Fig. 19, there exist far fewer dark blue speckles than in Fig. 6. This suggests that a number of locations in Set #1 had access blocked locally by small, sharp terrain features.

Sun access is again more evenly distributed across the map than Earth access. However, the maximum Sun access is significantly higher than in Set #1. With the +1 m altitude, the maximum Sun access detected is 89.2%, on the ridgeline nearest Shackleton (the ridgeline on which the Pentagon is pictured in Fig. 18), at 89.4296°S, 137.2233°W. This percentage is 12.2% higher than in Set #1, indicating access on 44.5 days more out of the year.

Figure 20 shows the maximum duration of no-access, or eclipse, periods for the Sun and Earth. Its appearance is similar to that of Fig. 7, although significantly fewer "speckles" exist in the maps, again indicating the presence of areas with access blocked locally by small, sharp terrain features. While the shortest maximum Earth eclipse duration remains unchanged at approximately 11.71 days, the shortest maximum Sun eclipse on the map has been nearly halved from 6.10 days to 3.11 days (at a point near the rim of Shackleton Crater with 85.7% Sun access, at 89.7733°S, 155.7213°W).

2. Optimal Site Selection

Here, an optimal site is identified assuming the same user weights and filters as in Figure 8. The GUI decision-making tool is used, and the resulting suitability map is shown in Fig. 21. This plot is similar to the original 0 m altitude version in Fig. 9, but note that the optimal location has changed to the ridgeline nearest Shackleton, at 89.4296°S, 137.2233°W. Access statistics at this point are shown in Fig. 22. This site has Sun access 89.2% of the year (the highest value available on the map) and Earth access 58.1% of the year. The maximum duration for which the Sun is inaccessible is 9.2 days, and access is uninterrupted for 7.6 months (228.3 days) of the year. Earth access periods are regularly 15-16 days in duration, and Earth eclipse periods are regularly 11-12 days in duration.

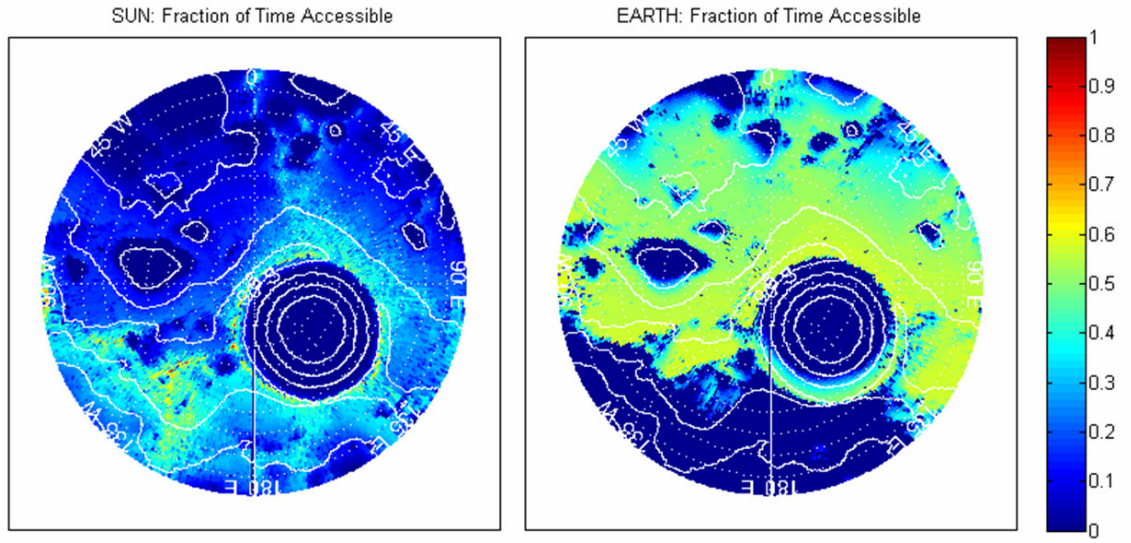

Figure 19. Maps of fraction of time with Sun access (left) and Earth access (right) for Set #2.
The northern extent of the map is 89°S, and contours indicate 1 km changes in terrain elevation.

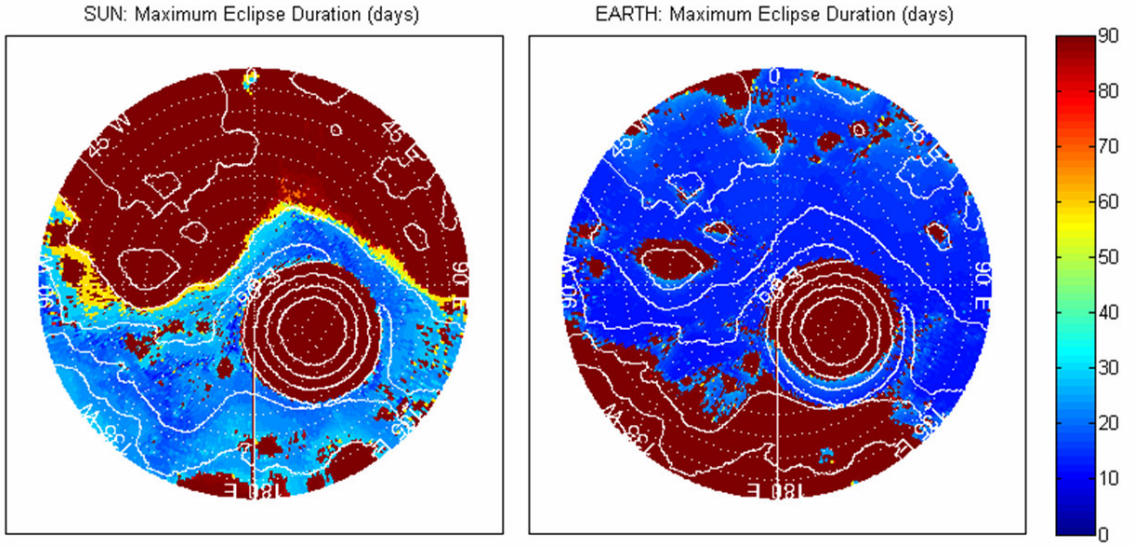

Figure 20. Maps of maximum time without Sun access (left) and Earth access (right) for Set #2.
The northern extent of the map is 89°S, and contours indicate 1 km changes in terrain elevation.

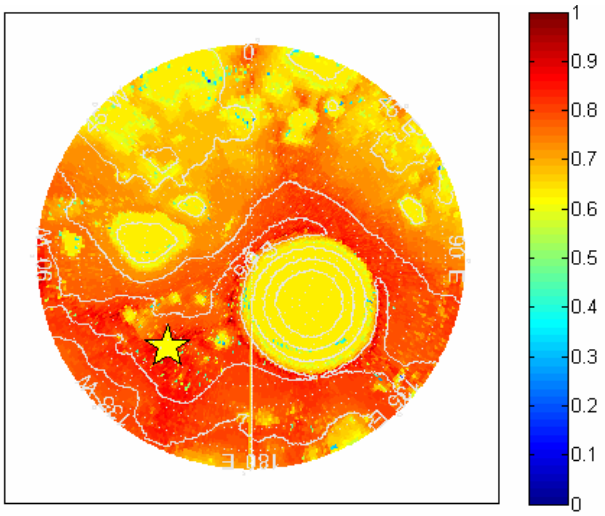

Figure 21. Map of site suitability with no filters for Set #2, using the weights in Fig. 8.
The yellow star indicates the optimum site for the selected weights. The northern extent of the map is 89°S, and contours indicate 1 km changes in terrain elevation.

Optimal Location Results
AHP Weighting Scheme

89.4296°S, 137.2233°W

58.1% Earth Access
89.2% Sun Access

Max Earth Eclipse:	12.1 days
Max Sun Eclipse:	9.2 days
Max Earth Access:	15.8 days
Max Sun Access:	228.3 days

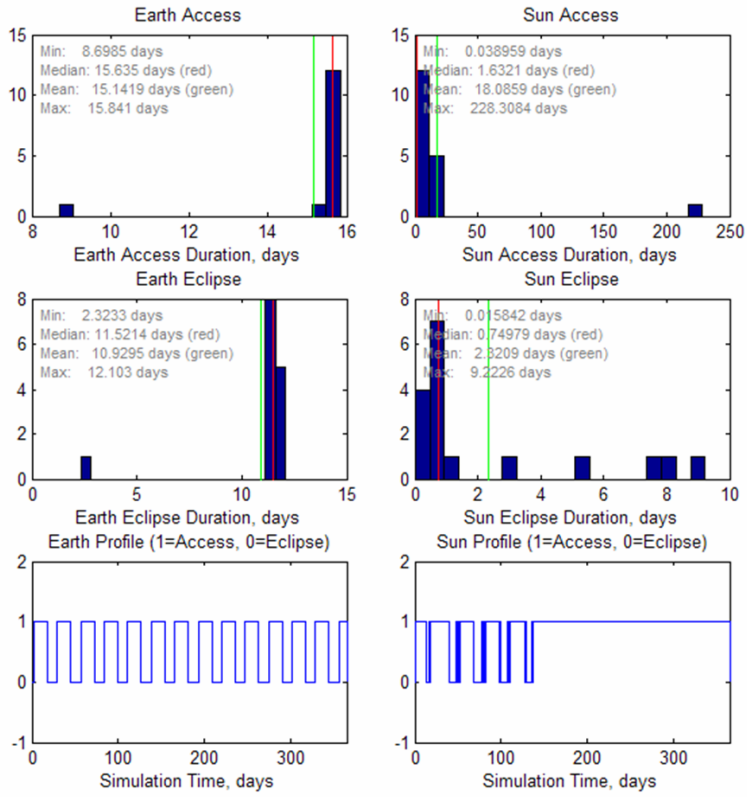

Figure 22. Detailed Earth and Sun access for the optimal location for Set #2 according to Fig. 8 weights.
The top plots are histograms of Earth and Sun access durations, the middle plots are histograms of Earth and Sun eclipse durations, and the bottom plots show simulation time histories of Earth and Sun access.

3. Pareto-Optimal Sites

For Set #2, the 32,384 data points are reduced to a set of 22 Pareto-optimal points. For a mission where access is to be considered +1 m altitude above the ground (e.g., a notional robotic mission), these 22 points are theoretically the only points that should be considered when examining trades among the six defined objectives. These points and their performance with respect to the six objectives are listed in Table 3.

The first 14 points in Table 3 are of greatest interest. Note that Point #2 near de Gerlache has the highest percent access to Earth and the minimum longest Earth eclipse period, just as it did when access was recorded at 0 m altitude. However, interestingly, the best Sun access metrics are no longer coincident at a single location. As mentioned earlier, the highest Sun access percentage is 89.2% on the ridge nearest Shackleton, a site with a maximum Sun eclipse duration of 9.2 days (Point #8). In contrast, the shortest maximum Sun eclipse duration is about three times shorter – at 3.1 days – on a location on the Shackleton rim (Point #11) that has a smaller Sun access percentage of 85.7%. Points #15-22 are technically Pareto-optimal because they have the best possible (zero) standard deviation for Sun or Earth eclipse duration. However, these points are again not of practical interest because the zero eclipse duration standard deviation is due to the fact that a single 365-day eclipse exists (i.e., the sites are in permanent eclipse, with no access to either Earth or the Sun).

Points #1-14 are clustered in the same four distinct geographic areas as the Pareto-optimal points for Set #1. The Pareto-optimal points for this particular set are shown in Fig. 23. Note the added cluster of points at the rim of Shackleton and the reduced cluster at the de Gerlache rim. Again, these clusters suggest that these geographic locations will consistently stand out regardless of the weights a user assigns to the six objectives.

Table 3. Pareto-Optimal Points for +1 m Altitude Access (Set #2).

Point No.	Latitude	Longitude	Percent Access		Max Eclipse (d)		Ecl. STDV (d)		Comments
			Sun	Earth	Sun	Earth	Sun	Earth	
1	89.0234°S	93.1126°W	71.1%	58.3%	9.05	11.73	1.95	2.59	
2	89.0234°S	92.4012°W	66.7%	58.3%	9.22	11.71	2.05	2.59	Max Earth Access Pct, Shortest Max Earth Eclipse
3	89.3202°S	113.7451°W	72.7%	57.5%	7.29	11.90	2.12	2.51	
4	89.3202°S	113.0336°W	45.3%	57.5%	20.29	11.88	6.54	2.50	
5	89.3515°S	112.3221°W	50.1%	57.4%	8.02	11.93	2.64	2.50	
6	89.4140°S	113.7451°W	49.2%	57.3%	12.56	12.03	3.36	2.50	
7	89.4140°S	113.0336°W	31.8%	57.3%	22.62	12.05	8.36	2.50	
8	89.4296°S	137.2233°W	89.2%	58.1%	9.22	12.10	3.11	2.49	Max Sun Access Pct, Opt. in Figs. 21-22
9	89.4296°S	136.5119°W	72.2%	58.1%	11.23	12.09	4.06	2.49	Min Nonzero Earth Eclipse STDV
10	89.4765°S	136.5119°W	85.7%	58.1%	4.42	12.12	1.21	2.49	
11	89.7733°S	155.7213°W	85.7%	57.2%	3.11	12.65	0.79	2.56	Shortest Max Sun Eclipse
12	89.7733°S	155.0099°W	84.6%	57.2%	3.73	12.66	0.91	2.56	
13	89.7733°S	154.2984°W	84.4%	57.2%	3.11	12.66	0.82	2.56	
14	89.7733°S	153.5870°W	85.4%	57.2%	3.16	12.64	0.78	2.56	Min Nonzero Sun Eclipse STDV
15	89.1640°S	26.9466°W	0.0%	43.4%	365.00	15.77	0.00	3.13	Permanent Sun Eclipse
16	89.8202°S	39.7530°W	0.0%	44.0%	365.00	15.77	0.00	3.07	Permanent Sun Eclipse
17	89.8358°S	49.0020°W	0.0%	44.0%	365.00	15.78	0.00	3.10	Permanent Sun Eclipse
18	89.3046°S	145.0494°W	59.2%	0.0%	14.25	365.00	3.55	0.00	Permanent Earth Eclipse
19	89.3046°S	142.9150°W	49.0%	0.0%	16.60	365.00	3.45	0.00	Permanent Earth Eclipse
20	89.3046°S	139.3577°W	49.4%	0.0%	16.84	365.00	3.52	0.00	Permanent Earth Eclipse
21	89.3202°S	143.6265°W	62.4%	0.0%	13.97	365.00	3.62	0.00	Permanent Earth Eclipse
22	89.9608°S	63.9427°W	9.9%	0.0%	27.56	365.00	3.15	0.00	Permanent Earth Eclipse

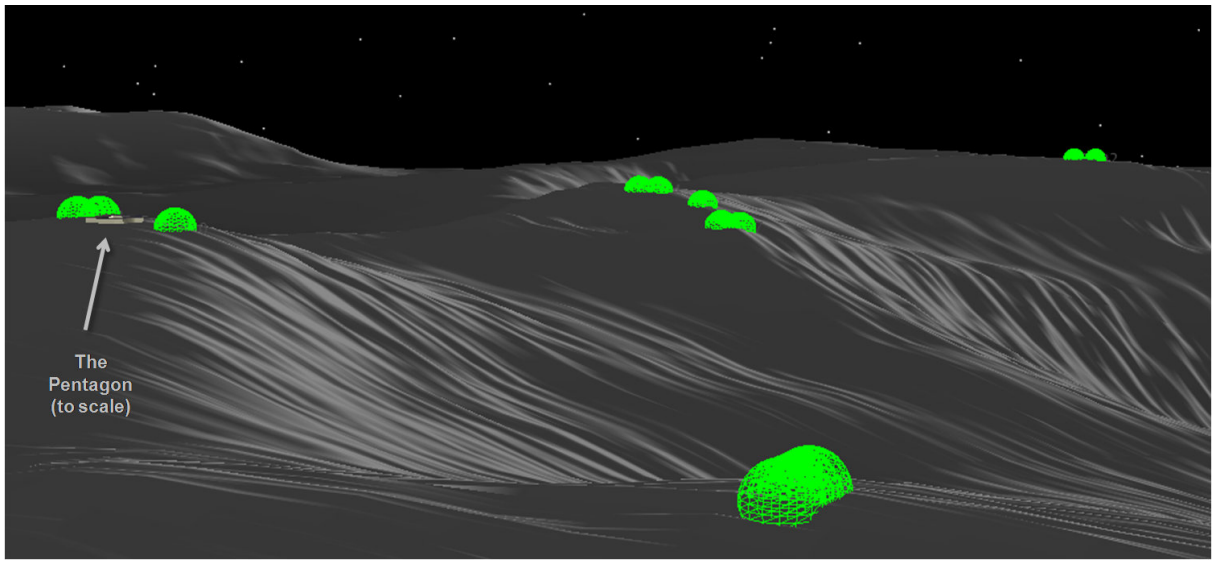

Figure 23. STK visualization of the Pareto-optimal locations for the +1 m Access condition (Set #2).
The camera in this image is positioned above Shackleton Crater. Points #15-22 are excluded.

D. Set #3: +10 m Notional Human Mission Results

Presented here are results from Set #3, the analysis set that considers access as assessed ten meters above the surface. This is intended to be more realistic for antenna or solar array placement conditions for human-class missions, and tracking access at this elevated altitude mitigates the effects of small but sharp terrain features that could obstruct viewing locally. As with Sets #1-2, covered first are maps of the traditional access rates (fraction of time with access) as well as maps of maximum eclipse durations. Next, the site selection and decision tool is used to determine an optimal site for a given set of user weights. Following this is an identification of Pareto-optimal sites for this scenario.

1. Access and Eclipse Metric Maps

Figure 24 shows the fraction of time that the Sun and Earth are accessible at the +10 m altitude. Just as with the surface data shown in Fig. 6 and +1 m data shown in Fig. 19, Shackleton Crater is clear in both maps, as are other depressions that prevent visibility to both Sun and Earth. Earth access is again bimodally distributed across the map, with large portions of the map having high Earth access and others having virtually no access. There is no substantial change in the optimum Earth access condition with the raised altitude: The highest Earth access percentage is once again 58.3%, located at same location on the rim of de Gerlache at 89.0234°S, 92.4012°W. However, note that blue speckles in the right plot of Fig. 24 are virtually gone in comparison to Figs. 6 and 19. This again suggests that a number of locations in Sets #1-2 had access blocked locally by small, sharp terrain features.

Compared to the surface and +1 m altitude, Sun access for the +10 m altitude is significantly different. Many more yellow and red points are visible in the left plot of Fig. 24 compared to Figs. 6 and 19. The locations of these points correspond to the same four Pareto-optimal geographic areas identified for Sets #1-2, i.e., the rims of Shackleton and de Gerlache as well as the two ridgelines on the connecting terrain. The maximum Sun access detected is 93.1%, about four percent more than in Set #2, on the same ridgeline nearest Shackleton, at 89.4296°S, 137.2233°W.

Figure 25 shows the maximum duration of eclipse periods for the Sun and Earth. Its appearance is similar to that of Figs. 7 and 20, although significantly fewer “speckles” exist in the maps, again indicating the presence of areas with access blocked locally by small, sharp terrain features. Interestingly, in the left plot of Sun maximum eclipse duration, a clear “trail” of dark-blue, minimum-eclipse-duration points, exists between de Gerlache and Shackleton and could form a promising traverse route between the two craters. The shortest maximum Earth eclipse duration remains practically unchanged at 11.70 days, and the shortest maximum Sun eclipse on the map has been reduced from 3.11 days (in Set #2) to 2.99 days.

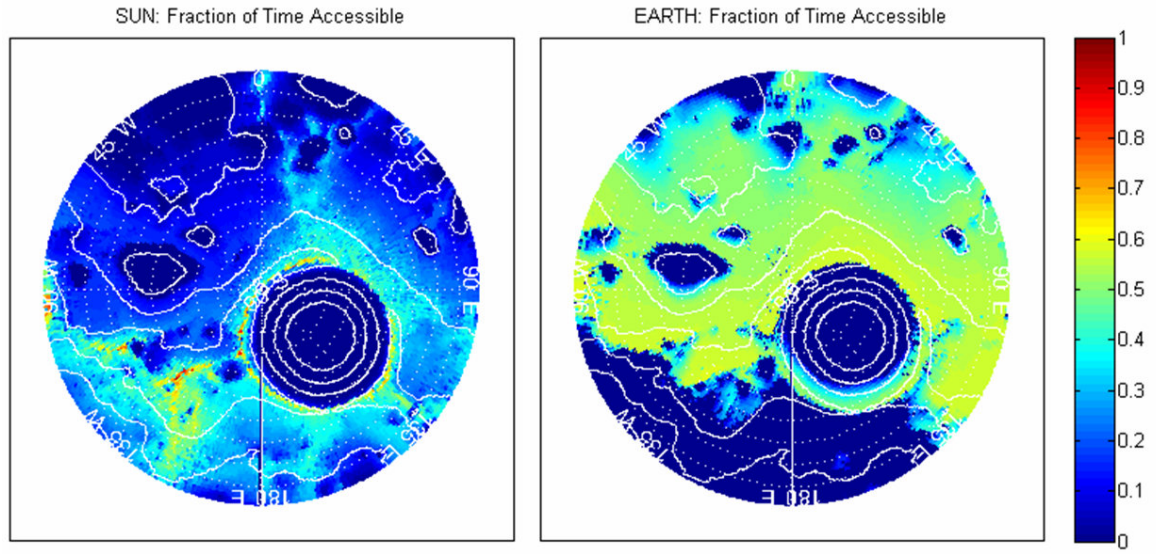

Figure 24. Maps of fraction of time with Sun access (left) and Earth access (right) for Set #3.
The northern extent of the map is 89°S, and contours indicate 1 km changes in terrain elevation.

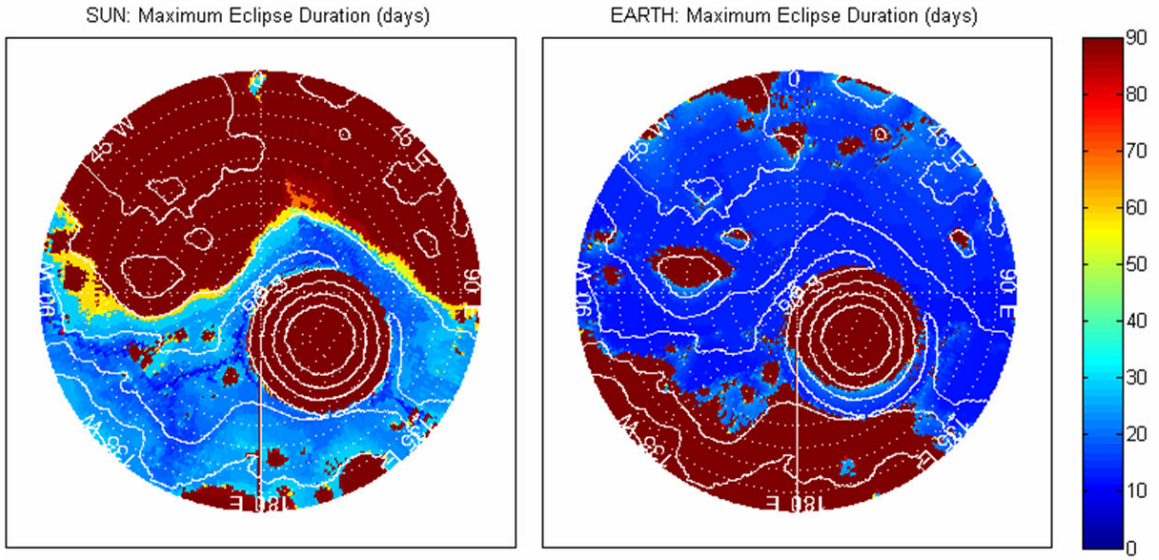

Figure 25. Maps of maximum time without Sun access (left) and Earth access (right) for Set #3.
The northern extent of the map is 89°S, and contours indicate 1 km changes in terrain elevation.

2. Optimal Site Selection

Here, an optimal site is identified assuming the same user weights and filters as in Figure 8. Using the GUI decision-making tool is used, the resulting suitability map is shown in Fig. 26. This plot is similar to the +1 m altitude plot in Fig. 21 and is distinguished by slightly higher suitability over the entire map and fewer "speckles" due to fewer local access blockages at the +10 m altitude. The optimal location is identical to the optimal location in Fig. 21, on the ridgeline nearest Shackleton at 89.4296°S, 137.2233°W. Access statistics at this point are shown in Fig. 27. With the +10 m altitude, this site has Sun access 93.2% of the year (the highest value available on the map) and Earth access 58.1% of the year. The maximum duration for which the Sun is inaccessible is 3.8 days, and access is uninterrupted for 7.6 months (228.3 days) of the year. Earth access periods are regularly 15-16 days in duration, and Earth eclipse periods are regularly 11-12 days in duration.

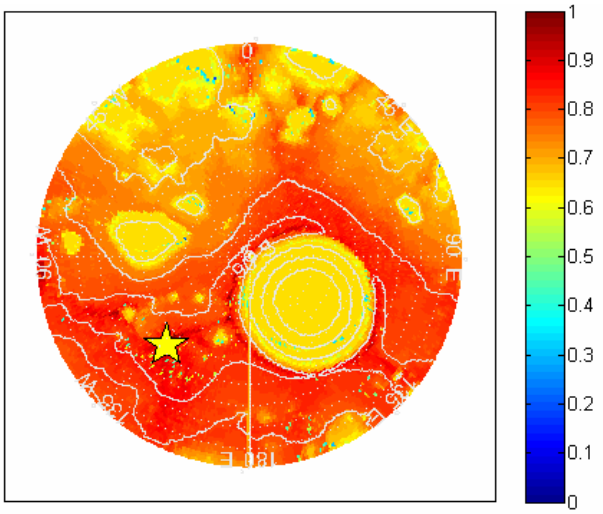

Figure 26. Map of site suitability with no filters for Set #3, using the weights in Fig. 8.
The yellow star indicates the optimum site for the selected weights. The northern extent of the map is 89°S, and contours indicate 1 km changes in terrain elevation.

Optimal Location Results
AHP Weighting Scheme

89.4296°S, 137.2233°W

58.1% Earth Access
93.1% Sun Access

Max Earth Eclipse: 12.1 days
Max Sun Eclipse: 3.8 days

Max Earth Access: 15.8 days
Max Sun Access: 228.3 days

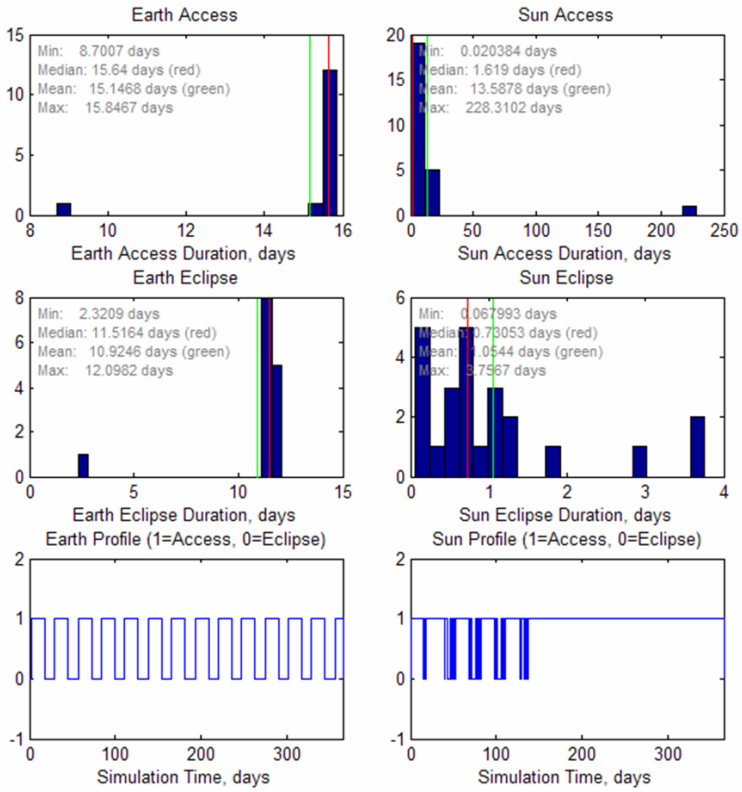

Figure 27. Detailed Earth and Sun access for the optimal location for Set #2 according to Fig. 8 weights.
The top plots are histograms of Earth and Sun access durations, the middle plots are histograms of Earth and Sun eclipse durations, and the bottom plots show simulation time histories of Earth and Sun access.

3. Pareto-Optimal Sites

For Set #3, the 32,384 data points are reduced to a set of 27 Pareto-optimal points. For a mission where access is to be considered +10 m altitude above the ground (e.g., a notional human mission), these 27 points are theoretically the only points that should be considered when examining trades among the six defined Sun and Earth access objectives. These points and their performance with respect to the six objectives are listed in Table 4.

The first 19 points in Table 4 are of greatest interest, and they are clustered in the same four distinct geographic areas as the Pareto-optimal points for Sets #1-2. Note that Point #3 near de Gerlache has the highest percent access to Earth and the shortest maximum Earth eclipse period, just as it did when access was recorded at 0 m and +1 m altitude. Also, similar to the Pareto-optimal results of Set #2, the maximum Sun access percentage (93.1%) occurs on the ridgeline nearest to Shackleton while the site of shortest maximum Sun eclipse duration (2.99 days) is on the southeastern rim of Shackleton. The key difference between Set #2 and Set #3, however, is that the maximum Sun eclipse duration at the ridgeline site is reduced to 3.76 days instead of 9.2 days. The Shackleton rim site has a Sun access percentage of 86.8%, so the major trade in terms of Sun access is 6.3% in access rate versus a shortening of the maximum eclipse time by 0.77 days. Points #20-27 are technically Pareto-optimal because they have the best possible (zero) standard deviation for Sun or Earth eclipse duration. However, these points are again not of practical interest because the zero eclipse duration standard deviation is due to the fact that a single 365-day eclipse exists (i.e., the sites are in permanent eclipse, with no access to either Earth or the Sun).

Table 4. Pareto-Optimal Points for +10 m Altitude Access (Set #3).

Point No.	Latitude	Longitude	Percent Access		Max Eclipse (d)		Ecl. STDV (d)		Comments
			Sun	Earth	Sun	Earth	Sun	Earth	
1	89.0234°S	95.2470°W	79.7%	58.1%	8.76	11.87	1.89	2.60	
2	89.0234°S	93.1126°W	73.6%	58.3%	9.02	11.73	1.92	2.59	
3	89.0234°S	92.4012°W	72.4%	58.3%	9.19	11.70	1.91	2.59	Max Earth Access Pct, Shortest Max Earth Eclipse
4	89.2890°S	113.7451°W	78.2%	57.5%	9.38	11.89	2.74	2.52	
5	89.3046°S	113.7451°W	76.9%	57.5%	9.56	11.89	2.70	2.51	
6	89.3202°S	113.7451°W	76.8%	57.5%	7.26	11.89	2.01	2.51	
7	89.3202°S	113.0336°W	60.1%	57.6%	16.79	11.88	4.63	2.50	
8	89.3515°S	112.3221°W	51.3%	57.4%	8.00	11.92	2.61	2.50	
9	89.4140°S	114.4565°W	48.9%	57.4%	12.22	12.03	3.41	2.50	
10	89.4140°S	113.7451°W	50.4%	57.3%	12.14	12.03	3.24	2.50	
11	89.4296°S	137.2233°W	93.1%	58.1%	3.76	12.10	1.01	2.49	Max Sun Access Pct, Opt. in Figs. 26-27
12	89.4296°S	136.5119°W	86.6%	58.2%	9.56	12.08	3.37	2.49	
13	89.4296°S	135.8004°W	48.3%	58.1%	16.74	12.11	7.04	2.49	Min Nonzero Earth Eclipse STDV
14	89.4452°S	137.2233°W	90.2%	58.1%	4.28	12.11	1.03	2.49	
15	89.4765°S	136.5119°W	90.6%	58.1%	3.65	12.12	0.94	2.49	
16	89.7733°S	155.7213°W	87.1%	57.2%	3.00	12.65	0.75	2.56	
17	89.7733°S	155.0099°W	86.8%	57.2%	3.02	12.65	0.75	2.56	
18	89.7733°S	154.2984°W	86.8%	57.2%	2.99	12.65	0.75	2.56	Shortest Max Sun Eclipse
19	89.7733°S	153.5870°W	86.7%	57.2%	3.02	12.63	0.74	2.56	Min Nonzero Sun Eclipse STDV
20	89.0077°S	69.8123°E	0.0%	43.7%	365.00	15.80	0.00	3.11	Permanent Sun Eclipse
21	89.1640°S	26.9466°W	0.0%	43.7%	365.00	15.67	0.00	3.12	Permanent Sun Eclipse
22	89.6796°S	51.8478°W	0.0%	43.2%	365.00	16.02	0.00	3.10	Permanent Sun Eclipse
23	89.1640°S	151.4526°W	57.2%	0.0%	13.93	365.00	5.76	0.00	Permanent Earth Eclipse
24	89.3046°S	145.0494°W	61.2%	0.0%	14.04	365.00	3.60	0.00	Permanent Earth Eclipse
25	89.3046°S	142.9150°W	52.6%	0.0%	15.87	365.00	3.45	0.00	Permanent Earth Eclipse
26	89.3202°S	143.6265°W	63.3%	0.0%	13.95	365.00	3.66	0.00	Permanent Earth Eclipse
27	89.3359°S	142.2036°W	60.1%	0.0%	14.01	365.00	3.47	0.00	Permanent Earth Eclipse

IV. Conclusions

This paper has provided a systematic analysis of Earth and Sun access for the lunar south pole region surrounding Shackleton Crater. Following a brief literature review, the data generation process using the Global Mapper, STK, and MATLAB software packages was discussed. The model outputs were then compared to the illumination rate results of Ref. 18 and showed acceptable agreement. Analysis consisted of three scenarios with different altitudes above the surface at which to track access, accounting for the fact that practical human or robotic landers and rovers will have antennas or solar arrays elevated some height above the surface. For each scenario, the percentage of available Sun and Earth access and maximum eclipse durations were mapped. Next, six metrics of interest were combined into a suitability score using the TOPSIS multi-attribute decision-making technique, and optimal locations were identified. Finally, Pareto-optimal sites, which do not depend on user weighting preferences, were identified, effectively reducing the number of site options from over 32,000 to just 20-30 candidates.

A. Tools and Methods

Perhaps the most important outcome of this effort is that it has resulted in a comprehensive capability to model and systematically analyze lunar south pole access. This capability is extensible well beyond the data and considerations in this study. When new lunar terrain data becomes available from future projects or missions (such as NASA's Lunar Reconnaissance Orbiter), the STK model can be updated with the most current data. The STK model also allows tracking of access between any objects in the scenario of interest; as designs and plans mature, access between lunar ground sites and orbiting relay satellites or specific Deep Space Network ground sites can be tracked. The STK model is also applicable to non-polar sites, provided topography data is available.

The MATLAB decision and site selection GUI may also provide a useful capability for future analyses. This tool is separate from the STK model, and it is not limited to reading STK's outputs. Users can easily format their own Earth and Sun access data to be read by the GUI and then use the GUI to apply weights and filters in order to visualize the suitability of the terrain and identify optimal landing or outpost sites. The GUI is not limited to the south pole region and can be easily adapted for use elsewhere. Furthermore, if the user wishes to consider additional terrain-related properties as objectives or constraints, such as slope, rock count, or distance to the nearest point of interest, these attributes are relatively easily to integrate.

B. Landing/Outpost Site Recommendations

This analysis has effectively narrowed the list of preferred landing or outpost sites to a handful of points concentrated in four geographic regions spaced 9-15 km apart. As shown in Table 5 and Fig. 28, these regions are (1) the southeastern rim of Shackleton Crater, (2) a ridgeline approximately in line with the 136°W meridian, (3) a ridgeline approximately in line with the 112°W meridian, and (4) the southern rim of de Gerlache Crater.

Two of these regions, the 136°W ridgeline and the southeastern Shackleton rim, are of particular interest. According to the nominal AHP weighting scheme used here, the rim region was optimal at the 0 m altitude, but the ridgeline region was optimal for the more realistic +1 m and +10 m altitudes. Ridgeline Sun access at the +10 m altitude reached 93.1%, with an uninterrupted access period of over 7 months and maximum eclipse period of 3.8 days. At the same +10 m altitude, Shackleton rim Sun access is about 86.8% with a 5-month uninterrupted period but also a shorter maximum eclipse period of 2.99 days, indicating eclipses due to terrain obscuration are more frequent but shorter in duration than at the ridgeline region. Earth access is regular at both sites and varies in availability by only about 1%.[‡‡] It is recommended that both of these regions be considered as potential sites in future analyses. Additional factors distinguishing these two regions, such as proximity to Shackleton Crater, surface slope, and rock count, may be more significant in this decision than the access differences seen here.

Table 5. Approximate Coordinates of Consistently Optimal Regions.

Region	Approx. Location		Elevation	Distance from Shackleton Center
	Latitude	Longitude		
Southeastern Shackleton Rim	89.77°S	154.44°W	1.684 km	10.4 km
Western Ridgeline	89.43°S	136.51°W	1.919 km	20.9 km
Eastern Ridgeline	89.30°S	112.32°W	1.603 km	26.6 km
Southern de Gerlache Rim	89.02°S	92.40°W	1.474 km	37.4 km

[‡‡] In general in this study, Earth access matters primarily in terms of whether it exists or not; sites with Earth access tend to have it regularly and 50-60% of the time, likely because Earth rises several degrees higher on the lunar south pole horizon than the Sun.

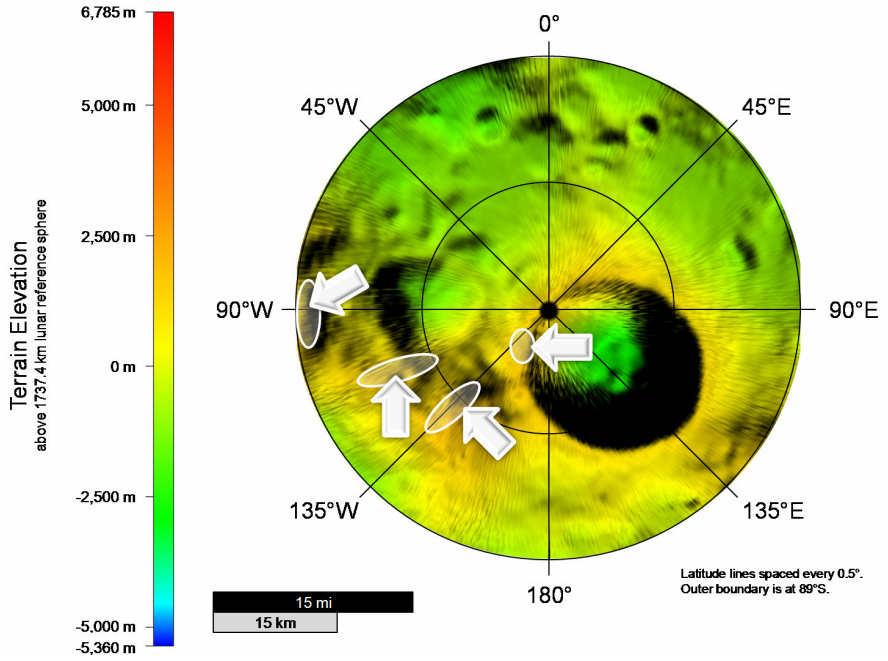

Figure 28. Locations of consistently optimal regions overlaid on Kaguya (SELENE) terrain data.

C. Influence of Solar Array and Antenna Altitudes

An important conclusion from this analysis is that access results (particularly for Sun access) can be very sensitive to small perturbations in the altitude at which the data is gathered. For example, at a site in the western ridgeline region, Sun access percentage rose from 75.0% at 0 m altitude to 89.2% at +1 m altitude (51.8 more days of access per year!) and to 93.1% at +10 m altitude (adding another 14.2 days per year). It is highly recommended that future studies consider this effect. It provides more realistic estimates in several respects. First, real missions will have elevated components, and in addition, adding this small elevation helps mitigate differences or shortcomings of modeling techniques and their terrain interpolation algorithms. Furthermore, the common convention of tracking access at 0 m can be misleading since detail about small-scale features such as boulders and small craters, which will have a large effect on 0 m surface access, is often not captured in the terrain data sets.

D. Future Enhancements

As noted earlier, the extensibility of the STK model and MATLAB decision tool makes a number of future enhancements possible. Among the most important is the inclusion of additional metrics for consideration in the MATLAB decision tool. An appropriate initial step might be the inclusion of metrics such as terrain slope and distances to points of interest. Also, an expansion of the analysis region north of 89°S would allow analysis of the Malapert range, for example, and allow a suitability comparison with the Shackleton region. Another step for the near future is analysis using higher-resolution terrain data from a study using the Goldstone Solar System Radar[30] or other data that will be released in the coming years. A number of possibilities exist for future use of this analysis and its methods and tools, and it is hoped this work will find broad use within the lunar mission design community.

Acknowledgments

This work would not have been possible without the help of several individuals. Most importantly, the authors would like to thank Dr. Hirotomo Noda of the National Astronomical Observatory of Japan (NAOJ) for sharing his illumination rate results, which led to several significant enhancements to the STK model in this work. Great thanks are also due to Nat Bachman, Chuck Acton, Barbara Wilson, Kelley Case, and Chuck Baker from NASA JPL for their invaluable advice and suggestions. Additional thanks are due to Lee Bryant, Jerry Condon, and Jeff Gutkowski at NASA JSC for their support in this effort, and final thanks are due to Chelsea Lewis and Sean Goodrich at JPL. Part of the research described in this paper was carried out at the Jet Propulsion Laboratory, California Institute of Technology, under a contract with the National Aeronautics and Space Administration.

References

[1]Bondre, N., "Shackleton grows older," *Nature Geoscience,* Vol. 1, No. 9, Sept. 2008, p. 573.

[2]Vasavada, A.R., Paige, D.A., and Wood, S.E., "Near-Surface Temperatures on Mercury and the Moon and the Stability of Polar Ice Deposits," *Icarus,* Vol. 141, No. 2, pp. 179-193.

[3]Urey, H.C., *The Planets, Their Origin and Development,* Yale University Press, New Haven, 1952, Chap. 2.

[4]Proctor, R.A., "Condition of the Moon's Surface," *The Quarterly Journal of Science,* Vol. 3, No. 37, pp. 29-55.

[5]Coakley, G.W., "The Disappearance of the Water and Atmosphere of the Moon," Papers read at the meetings of the American Astronomical Society, Brooklyn, Nov. 1884, pp. 1-8.

[6]Watson, K., Murray, B., and Brown, H., "On the Possible Presence of Ice on the Moon," *Journal of Geophysical Research,* Vol. 66, No. 5, May 1961, pp. 1598-1600.

[7]Watson, K., Murray, B., and Brown, H., "The Behavior of Volatiles on the Lunar Surface," *Journal of Geophysical Research,* Vol. 66, No. 9, Sept. 1961, pp. 3033-3045.

[8]Nozette, S., Lichtenberg, C.L., Spudis, P., Bonner, R., Ort, W., Malaret, E., Robinson, M., and Shoemaker, E.M., "The Clementine Bistatic Radar Experiment," *Science,* Vol. 274, Nov. 1996, pp. 1495-1498.

[9]Stacy, N.J.S., Campbell, D.B., and Ford, P.G., "Arecibo Radar Mapping of the Lunar Poles: A Search for Ice Deposits," *Science,* Vol. 276, June 1997, pp. 1527-1530.

[10]Binder, A.B., "Lunar Prospector: Overview." *Science,* Vol. 281, Sept. 1998, pp. 1475-1476.

[11]Feldman, W.C., Maurice, S., Binder, A.B., Barraclough, B.L., Elphic, R.C., and Lawrence, D.J., "Fluxes of Fast and Epithermal Neutrons from Lunar Prospector: Evidence for Water Ice at the Lunar Poles," *Science,* Vol. 281, Sept. 1998, pp. 1496-1500.

[12]Colaprete, A., Briggs, G., Ennico, K., Wooden, D., Heldmann, J., Sollitt, L., Asphaug, E., Korycansky, D., Schultz, P., Christensen, A., and Galal, K., "An Overview of the Lunar Crater Observation and Sensing Satellite (LCROSS) Mission – An ESMD Mission to Investigate Lunar Polar Hydrogen," Joint Annual Meeting of LEAG-ICEUM-SRR (LPI Contribution No. 1446), Cape Canaveral, 28-31 Oct. 2008.

[13]Colaprete, A., Delory, G., Wargo, M., and Cooke, D., LCROSS Science Briefing [televised NASA news conference], Moffett Field, 13 Nov., 2009.

[14]Spudis, P.D., Stockstill, K.R., Ockels, W.J., Kruijff, M, "Physical Environment of the Lunar South Pole from *Clementine* Data: Implications for Future Exploration of the Moon," *Abstracts of the Lunar and Planetary Science Conference,* Vol. 26, 1995, pp. 1339-1340.

[15]Bussey, D.B.J., Spudis, P.D., Robinson, M.S., "Illumination conditions at the lunar south pole," *Geophysical Research Letters,* Vol. 26, No. 9, May 1999, pp. 1187-1190.

[16]Margot, J.L., Campbell, D.B., Jurgens, R.F., and Slade, M.A., "Topography of the Lunar Poles from Radar Interferometry: A Survey of Cold Trap Locations," *Science,* Vol. 284, June 1999, pp. 1658-1660.

[17]Fincannon, J., "Lunar Polar Illumination for Power Analysis," AIAA 2008-5631, 6th International Energy Conversion Engineering Conference, Cleveland, 28-30 July 2008.

[18]Noda, H., Araki, H., Goossens, S., Ishihara, Y., Matsumoto, K., Tazawa, S., Kawano, N., and Sasaki, S., "Illumination conditions at the lunar polar regions by KAGUYA (SELENE) laser altimeter," *Geophysical Research Letters,* Vol. 35, Dec. 2008.

[19]Fincannon, J., "Lunar South Pole Illumination: Review, Reassessment, and Power System Implications," AIAA 2007-4700, 5th International Energy Conversion Engineering Conference and Exhibit, St. Louis, 25-27 June 2007.

[20]Grebow, D.J., Ozimek, M.T., and Howell, K.C., "Multibody Orbit Architectures for Lunar South Pole Coverage," *Journal of Spacecraft and Rockets,* Vol. 45, No. 2, March 2008. pp. 344-358.

[21]Ozimek, M.T., Grebow, D.J., and Howell, K.C., "Solar Sails and Lunar South Pole Coverage," AIAA 2008-7080, AIAA/AAS Astrodynamics Specialist Conference and Exhibit, Honolulu, 18-21 Aug. 2008.

[22]Malmström, R.W., Lo, A., Brown, N.S., and Haney, G., "Continuous Communications to the Moon's South Pole," AIAA 2006-7455, Space 2006, San Jose, 19-21 Sept. 2006.

[23]Gramling, J.J., Ngan, Y., Quinn, D.A., and Folta, D.C., "A Lunar Communications and Navigation Satellite Concept for the Robotic Lunar Exploration Program," AIAA 2006-5364, 24th AIAA International Communications Satellite Systems Conference, San Diego, 11-14 June 2006.

[24]Japan Aerospace Exploration Agency, *Result of KAGUYA: The lunar global and sectional topographic data* [online database]. URL: http://www.kaguya.jaxa.jp/en/science/LALT/The_lunar_topographic_data_e.htm [24 July 2009].

[25]USGS Astrogeology Research Program, *Gazetteer of Planetary Nomenclature* [online database]. URL: http://planetarynames.wr.usgs.gov/ [25 July 2009].

[26]Sharpe, B.L. and Schrunk, D.G., "An Operationally Ideal Location for the First Permanent Base on the Moon," *Proceedings of Space 2000: The Seventh International Conference and Exposition on Engineering, Construction, Operations, and Business in Space,* 2000, pp. 777-783.

[27]Lowman, P.D., Sharpe, B.L., Schrunk, D.G., "Moonbase Mons: Making the Case," *Aerospace America,* Vol. 46, No. 10, Oct. 2008. pp. 38-43.

[28]Saaty, T.L., *The Analytic Hierarchy Process,* McGraw-Hill, New York, 1980.

[29]Hwang, C. and Yoon, K., *Multiple Attribute Decision Making,* Springer-Verlag, Berlin, 1981.

[30]"NASA Scientists Bring Light to Moon's Permanently Dark Craters," Mission News, NASA, June 2009. URL: http://www.nasa.gov/topics/moonmars/features/dsn-20090618.html [31 July 2009].